Manipulating Quantum Dot Nanostructures for Photonic and Photovoltaic Applications

by

Andrew Martin

A dissertation submitted in partial fulfillment of the requirements for the degree of Doctor of Philosophy (Materials Science and Engineering) in the University of Michigan 2013

Doctoral Committee:

Professor Joanna Mirecki-Millunchick
Assistant Professor Emmanouil Kioupakis
Associate Professor Jamie Dean Phillips
Assistant Professor Vanessa Sih

© Andrew J. Martin 2013

DEDICATION

This work is dedicated to my parents, Jim and Elise, my siblings, Allison, David, and Meredith, and to my wife, Melissa. Without their impact on my life, shaping me into who I am and encouraging all my efforts, this work would not have been possible.

ACKNOWLEDGMENTS

First and foremost, I would like to acknowledge my Ph.D. advisor, Prof. Joanna Millunchick. Upon leaving Purdue University to begin graduate work at the University of Michigan, I had the opportunity to speak with former Purdue President Martin Jischke. I asked President Jischke what to look for in a Ph.D. advisor and his advice to me was to find someone with similar values to myself. I stuck by this advice and it has never steered me wrong. After three years of working under Joanna, I told her that choosing her as an advisor was one of the best decisions I have ever made. Joanna has helped me mature as a researcher, engineer, and person. She has helped me improve my writing skills, my knowledge of complex equipment, and encouraged me to reach my potential. Joanna has also helped me realize and develop my strengths and skills, and I am very grateful for that.

The studies presented in this work have been highly collaborative. Both the quantity and quality of this work are due in large part to the excellent minds and skills of those who helped along the way in many different ways. I am very grateful to my former lab mates who helped train me on our own lab equipment and other analytical techniques, which I have used for much of this work. A special thanks is due to Dr. Jessica Bickel, Dr. Jenny Lee-Feldman, and Dr. Kevin Grossklaus, from whom I learned so much. I also need to recognize my current lab mates Adam Duzik and Matt DeJarld who have helped me with experiments over the past two years.

Much credit is due to Prof. Vanessa Sih and her research group in Physics including Timothy Saucer, Jieun Lee, and Garrett Rodriguez who have been co-authors on over a half

dozen peer-reviewed articles with me. Their excellent work has made mine much easier. Other collaborators who deserved acknowledgement are Sung Joo Kim, Prof. Xiaoqing Pan, Dr. Guang Ran, Dr. Kai Sun, Dr. Allen Hunter, Prof. Emmanuelle Marquis, Dr. Jinyoung Hwang, Prof. Jamie Phillips, Erwin Smakman, Prof. Paul Koenraad, and, of course, the EMAL Staff.

I would also like to acknowledge the Center for Solar and Energy Conversion, which has funded this work. It has been a great experience to be a part of this center and to work with other great researchers within it. This material is based upon work supported as part of the Center for Solar and Thermal Energy Conversion, an Energy Frontier Research Center funded by the U. S. Department of Energy, Office of Science, Office of Basic Energy Sciences under Award Number DE-SC0000957. Transmission electron microscopy work in this paper is supported by NSF DMR-0723032. I would also like to acknowledge Prof. Thomas O'Haver at the University of Maryland for his peak-fitting program.

I would also like to acknowledge the men of my gradCRU Bible study over the past three and a half years since I started my work at Michigan. These men have been a constant encouragement to me, and a continual reminder of what really matters in life. I have formed friendships with them that will last a lifetime, and they have helped me keep a work-life balance that allows me to approach my work with energy and excitement. My gradCRU Bible studies have been a constant reminder to me that my abilities and work are gifts from God that I can choose to use to his glory. To search out the mysteries God has created in order to understand them and to use them to benefit the world around me is truly "the glory of kings."

"It is the glory of God to conceal a matter;

to search out a matter is the glory of kings."

Proverbs 25:2

TABLE OF CONTENTS

DEDICATION ii

ACKNOWLEDGMENTS iii

LIST OF FIGURES x

ABSTRACT xvi

Chapter 1: Introduction and Background 1

1.1 Introduction 1

1.2 Objectives and Organization 2

1.3 Part I 4

1.4 Part II 5

1.5 Overview of III-V Semiconductor Quantum Dots 6

1.6 The Stranski-Krastanov Growth Mode 9

1.7 Overview of Molecular Beam Epitaxy 10

1.8 References 14

Chapter 2: Introduction to Experimental and Analytical Techniques 17

2.1 Reflective High-Energy Electron Diffraction 17

2.2 Focused Ion Beam Lateral Surface Patterning 20

2.3 Atomic Force Microscopy 22

2.4 Atom Probe Tomography 24

2.4.1 Background 24

2.4.2 Focused Ion Beam Lift-out 26

2.4.3 Atom Probe Tip Milling 30

2.4.4 Three-dimensional Data Reconstruction 35

2.5 Photoluminescence 37

2.6 References: 38

PART I: Analysis of InAs Quantum Dots Patterned by *In Vacuo* Focused Ion Beam 39

Chapter 3: Lateral Patterning of Multilayer InAs/GaAs(001) Quantum Dot Structures by *In Vacuo* Focused Ion Beam 40

3.1 Introduction 40

3.2 Experimental Procedure 42

3.3 Data Analysis 43

3.3.1 Effects of FIB Dwell Time on QD Dimensions and Pattern Fidelity 43

3.3.2 Determination of In Adatom Diffusion Length 48

3.3.3 Variation in Wetting Layer Thickness with Patterning Conditions 50

3.3.4 Mound Formation Upon Increased Layering 52

3.4 Conclusions 56

3.5 References 57

Chapter 4: Effects of Pre-Determined Lateral Separation on Quantum Dot Size and Dissolution 60

4.1 Introduction 60

4.2 Experimental Procedure 61
4.3 Data Analysis 62
4.3.1 Effects of FIB Pattern Spacing on QD Dimensions and Fidelity 62
4.3.2 Changes in Photoluminescence Energy as a Function of Pattern Spacing 64
4.3.3 QD Dissociation Due to Increasing Separation 67
4.3.4 Distinguishing Surface Diffusion Lengths via FIB Patterning 69
4.4 Conclusions 70
4.5 Applications of FIB-Patterned InAs Quantum Dots 70
4.6 References: 72

PART II: Analysis of the Growth, Structure, and Optoelectronic Properties of GaSb Quantum Dots 75

Chapter 5: Atom Probe Tomography Analysis of Different Modes of Sb Intermixing in GaSb Quantum Dots and Wells 76

5.1 Introduction 76
5.2 Experimental Procedure 77
5.3 Data Analysis 78
5.3.1 Photoluminescence of Quantum Dot and Well Structures 78
5.3.2 Sb Concentration Profiles for Buried Nanostructures 80
5.3.3 Analysis of Different Modes of Sb Intermixing 83
5.4 Conclusions 86
5.5 References 87

Chapter 6: Analysis of Defect-Free GaSb/GaAs(001) Quantum Dots Grown on the Sb-terminated (2x8) Surface 90

6.1 Introduction...90

6.2 Experimental Procedure...91

6.3 Data Analysis...93

6.3.1 Differences in QD Dimensions and Areal Density.....................................93

6.3.2 Analysis of Defect Free QD Structures 95

6.3.3 QD Photoluminescence Properties 97

6.3.4 Dissolution Dependence on Surface Reconstruction.................................99

6.4 Conclusions..100

6.5 References..101

Chapter 7: The Disintegration of GaSb/GaAs Nanostructures Upon Capping 103

7.1 Introduction..103

7.2 Experimental Procedure..105

7.3 Data Analysis..106

7.3.1 QD Dimensions and Photoluminescence..106

7.3.2 Two-dimensional Analysis of Buried Nanostructures...............................108

7.3.3 Three-dimensional Analysis by Atom Probe Tomography 109

7.3.4 Calculated Transition Energies of Disintegrated QDs..............................113

7.4 Conclusions..115

7.5 Applications of GaSb Quantum Dots 115

7.6 References..118

Chapter 8: Conclusions and Future Work 121

8.1 Summary and Conclusions 121

8.2 Future Work..123

8.3 References..127

LIST OF FIGURES

Figure 1.1: Plot of the band gap as a function of lattice parameter. Plot taken from Vurgaftman *et al*.[28] Colored lines added to show approximate ranges of different spectra of visible and infrared light. 7

Figure 1.2: Three-dimensional AFM image of a QD showing the general dimensions of self-assembled QDs. 8

Figure 1.3: A schematic of the main steps of the Stranski-Krastanov growth mode for self-assembled QD nucleation. 9

Figure 1.4: A schematic of the lab equipment used in these studies. The MBE chamber is connected *in vacuo* to the scanning tunneling microscope and the FIB. Image used with permission from Dr. Kevin Grossklaus. 11

Figure 1.5: A photograph of the MBE used for all film and QD growths in these studies. 12

Figure 1.6: Schematic of the MBE chamber used in these studies. The main cells used are shown with the exception of dopant cells. 13

Figure 2.1: RHEED images for (a) the x4 side of the As-terminated (2 x 4) surface reconstruction, (b) the x8 side of the Sb-terminated (2x8) surface reconstruction, (c) the 2x side of a smooth GaAs (2 x 4) surface reconstruction, and (d) a spotty reconstruction formed as a result of QD nucleation. 18

Figure 2.2: A schematic showing the changes in surface roughness and corresponding specular spot intensity during RHEED oscillations. Image adapted from Neave *et al.* and Ohring.[1,2] 19

Figure 2.3: A schematic of the Magnum FIB column used for patterning of InAs QDs. The source, lenses, aperature, and octupole plates are indicated. Image courtesy of Dr. Kevin Grossklaus. 21

Figure 2.4: Atomic force microscopy image of a square array of FIB-patterned holes prior to InAs QD nucleation on the patterned sites. 22

Figure 2.5: A schematic of the Cameca LEAP 4000X atom probe used in these studies showing the sample tip, local electrode, reflectron and detector. 25

Figure 2.6: Scanning electron microscope and focused ion beam images of (a) – (c) the Pt mask and cut-out steps. (d) End-on view of the "V"-shaped lift-out sample. (e) A schematic of the lift-out specimen showing the approximate dimensions and location of the area of interest with respect to the volume as a whole. (f) – (i) Scanning electron microscopy images of the lift-out process including (f) attaching the needle and lifting it out, (g) and (h) aligning the lift-out sample above the micro-tip, and (i) mounting and cutting each sample volume onto a separate microtip..26

Figure 2.7: Scanning electron microscope images of the tip shaping steps. (a) Initial Pt gluing on both sides of the sample. (b) Initial milling and (c) filling of any voids with Pt. (d) Final tip shaping to achieve a tip radius of ~ 50 nm with the features of interest generally within the first 200 nm from the apex of the tip. 32

Figure 2.8: A schematic illustrating the milling steps used to create the atom probe tips. Adapted from Gault *et al.*[5]..34

Figure 2.9: Examples of atom probe data reconstructed in three dimensions showing where the data comes from within the sample tip and examples of an iso-concentration surface highlighting a given percent of Sb in yellow. 36

Figure 2.10: A schematic of the recombination pathways of GaSb/GaAs QDs and wetting layer with a type-II band alignment..38

Figure 3.1: A schematic of the FIB-patterned six and 26 layer InAs/GaAs QD structures. Square arrays of FIB-milled holes were patterned at the substrate with pattern spacings of 0.25, 0.5, 1.0, and 2.0 μm each at FIB dwell times of 1.0, 3.0, 6.0, and 9.0 ms. 2.0 ML of InAs was deposited for the QDs for both samples. The GaAs spacer layer thicknesses were 20 and 18 nm for the six and 26 layer samples, respectively...43

Figure 3.2: Plots of (a) QD diameter as measured at the sixth layer and FIB-milled hole diameter as measured at the substrate of a separate sample; (b) QD height as measured at the sixth layer and FIB-milled hole depth as measured at the substrate of a separate sample; (c) pattern fidelity as a function of FIB dwell time. All data is for the 2.0 μm pattern spacing as measured on the uncapped surface of the six layer sample. 45

Figure 3.3: AFM images of the uncapped surface of the six layer sample for the 2.0 μm spacing patterns at FIB dwell times of (a) 1.0 ms, (b) 3.0 ms, (c) 6.0 ms, and (d) 9.0 ms. The inset in (a) shows a higher magnification image of the multi-dot nucleation and the inset in (d) shows the concave shape of the FIB pattern, which did not completely planarize upon layering for the 6.0 and 9.0 ms dwell times..46

Figure 3.4: AFM images of the uncapped surface of the six layer sample for the 9.0 ms FIB dwell time patterns at pattern spacings of (a) 0.25 μm, (b) 0.5 μm, (c) 1.0 μm, and (d) 2.0 μm. The insert in (a) and (d) show higher magnification

images of the QDs. The concave shape of the holes (small, dark area beside the QDs) is shown to persist through to the sixth layer. (e) and (f) Plots of the QD diameter and height as a function of pattern spacing for the 9.0 ms FIB dwell time patterns of the six layer sample. 48

Figure 3.5: Schematics showing the change in the capture zone for (a) close pattern spacings and (b) larger pattern spacings. (c) A schematic of the ellipsoid and cylinder shapes used to approximate the QD volume for the wetting layer thickness estimation....50

Figure 3.6: AFM images of the uncapped surface of the 26 layer sample for the 9.0 ms FIB dwell time patterns at pattern spacings of (a) 0.25 µm, (b) 0.5 µm, (c) 1.0 µm, and (d) 2.0 µm with a corresponding histogram of QD diameter distribution below each AFM image. The insets in (c) and (d) show higher magnification images of the mounds with QDs on them. The number of bins for each histogram was determined by the square root of the number of data points. 53

Figure 3.7: Plot of the QD areal density as a function of pattern spacing as measured on the uncapped surface of the 26 layer sample for the 9.0 ms FIB dwell time. Error bars are not visible for all data points due to a small standard deviation for some of the measurements. The dashed and solid lines are explained in the text. 55

Figure 3.8: Photoluminescence spectrum from the 26 layer sample for the 9.0 ms FIB dwell time patterns showing the GaAs substrate peak at 1.49 eV, the wetting layer peak at 1.43 eV, and the QD peak between 1.27 and 1.35 eV. The split QD peak is a result of the bimodal QD distribution. The peak positions for the split QD peak are indicated by the tick marks. Measurements were taken at 15 K. Data collected by Timothy W. Saucer and Garrett V. Rodriguez, Prof. Vanessa Sih group, Physics Department, University of Michigan....56

Figure 4.1: Atomic force microscope image of the top layer of a six-layer stack of quantum dots patterned with a 10 pA, 30 keV Ga^+ *in vacuo* focused ion beam with a 9.0 ms dwell time and a 2.0 µm pattern spacing. 63

Figure 4.2: Plot of quantum dot diameter and height for the 9.0 ms dwell time patterns as a function of pattern spacing. Note that the height data points are offset slightly in *x* to more clearly display the data. 64

Figure 4.3: Photoluminescence data for the 9.0 ms dwell time patterns at each pattern spacing and for the unpatterned regions. Measurements were taken at 15 K and 101 µW laser power. The GaAs substrate peak is at 1.48 eV, the wetting layer peak ranges from 1.43 to 1.45 eV, and the QD peak ranges from 1.34 to 1.39 eV dependent on the pattern spacing. Data collected by Timothy W. Saucer, Prof. Vanessa Sih group, Physics Department, University of Michigan....65

Figure 4.4: Plots of (a) wetting layer and (b) quantum dot photoluminescence peak energy as a function of pattern spacing for each dwell time. The dashed line in (a) shows the peak energy for the unpatterned region...66

Figure 4.5: Plots of (a) wetting layer and (b) quantum dot photoluminescence peak intensity relative to the GaAs peak intensity as a function of pattern spacing for each dwell time. 67

Figure 4.6: Schematics of the different types of photonic crystals. Image taken from Igor *et al.*[22] 71

Figure 4.7: Enhancement of photoluminescence from quantum dots embedded in a photonic crystal. Spectra were measured at a laser power of 190 μW. The blue dashed line is a Lorentzian fit. The inset is a scanning electron microscope image of the photonic crystal. Figure adapted from Lee *et al.*[5] 72

Figure 5.1: Photoluminescence spectra from (a) a 1.0 ML GaSb quantum well, (b) a 1.5 ML GaSb quantum well, and (c) a 2.3 ML GaSb QD structure showing QD emission at 1.15 eV and a wetting layer peak at 1.36 eV. All intensities are normalized to the GaAs peak intensity, which is at approximately 1.45 eV. Photoluminescence specta collected by Timothy W. Saucer and Garrett V. Rodriguez, Prof. Vanessa Sih group, Physics. 79

Figure 5.2: Three-dimensional reconstructions of atom probe tomography data for (a) a 1.0 ML quantum well and (b) a 1.5 ML GaSb quantum well. The Sb atoms are shown in blue. The Sb concentration profile for each structure is shown to the left of the three-dimensional reconstruction. Sb concentration profiles are taken from a 10 nm cylinder with a 0.2 nm bin size through the center of the structures, perpendicular to the GaSb layers. APT data collected by Dr. Allen H. Hunter, Prof. Emmanuelle Marquis group, MSE. 81

Figure 5.3: Sb concentration profiles for the 1.0 ML and 1.5 ML quantum wells and the wetting layer in the 2.3 ML QD sample. All Sb concentration profiles are taken using a 10 nm diameter area and a bin size of 0.2 nm, perpendicular to the GaSb layers. Solid lines are fits to the Sb concentration profiles.........................82

Figure 5.4: (a) A three-dimensional reconstruction of atom probe tomography data from the 2.3 ML QD sample showing one compact QD and one disintegrated cluster of smaller islands with a 14% Sb concentration surface highlighted in yellow. (b) Sb concentration profiles through the QD, cluster, and wetting layer. The profiles for the QD and wetting layer were taken using a 10 nm diameter area and a bin size of 0.2 nm, perpendicular to the GaSb layer. The profile for the cluster was taken using a 4 nm diameter only through the small GaSb islands. Solid lines are fits to the Sb concentration profiles. The inset shows a top-down view of the GaSb nanostructures analyzed. APT data collected by Prof. Emmanuelle Marquis, MSE. 86

Figure 6.1: Reflective high energy electron diffraction patterns along [$\bar{1}$10] for (a) the As-terminated (2x4) surface reconstruction and (b) the Sb-terminated (2x8) surface reconstruction. 92

Figure 6.2: AFM images of the uncapped 11th layer of QDs grown on (a) the (2x4) surface and (b) the (2x8) surface showing the difference in QD size, shape, and areal density for dots grown on the different starting surface reconstructions. The height scale is 8 nm. 94

Figure 6.3: (a) and (b) Bright field TEM and high resolution HAADF images of QDs grown on the As-terminated (2x4) surface, respectively. (c) and (d) Bright field TEM and high resolution HAADF images of QDs grown on the Sb-terminated (2x8) surface, respectively. The HAADF images show a defect-free QD/spacer layer interface for both samples. Images taken by Dr. Guang Ran, Prof. Lumin Wang group, and Sung Joo Kim, Prof. Xiaoqing Pan group, MSE Department. 96

Figure 6.4: PL spectra taken at 10 K for the multilayer samples grown on (a) the (2x4) surface and (b) the (2x8) surface. The GaAs peak is at 1.48 eV and the WL peak is at 1.35 eV. There is a split QD peak is at 1.13 and 1.18eV, which may be due to quantum ring formation upon capping. There are also two low energy peaks at 0.97 and 1.07 eV, which we attribute to exciton emission. Gaussian peak fits are show for the QD (1.13 eV) and WL (1.18 eV) peaks. Data collected by Timothy W. Saucer and Garrett V. Rodriguez, Prof. Vanessa Sih group, Physics Department. Peak fitting program developed by Prof. Thomas O'Haver, University of Maryland. 98

Figure 6.5: AFM images of QDs from the single layer samples grown on (a) the (2x4) surface and (b) the (2x8) surface showing the resulting QD morphology after quenching in the absence of a group V overpressure. The height scale is 6 nm. 100

Figure 7.1: (a) AFM image of the uncapped GaSb/GaAs QDs. (b) and (c) Histograms of the QD diameter and height size distributions, respectively, for the uncapped QDs. 107

Figure 7.2: PL taken at 10 K and 424.5 μW of the GaSb/GaAs QDs showing the GaAs substrate peak at 1.49 eV, the WL peak at 1.36 eV, and the QD peak centered between 1.1 and 1.22 eV. The solid and dashed red arrows indicate the peak positions calculated for large compact QDs (1.155 eV) and small, disintegrated islands (1.220 eV) using an 8-band **k.p** method where approximate nanostructure dimensions are taken from the APT data. The inset shows the recombination pathways for the GaSb QDs, GaSb WL, and GaAs. Data collected by Timothy W. Saucer and Garrett V. Rodriguez, Prof. Vanessa Sih group, Physics Department, University of Michigan. 107

Figure 7.3: XSTM images of the GaSb/GaAs nanostructures looking at (110) surfaces showing (a) a compact QD, (b) – (e) clusters of smaller islands with varying separation and degrees of As-Sb intermixing between the islands. Images taken by Erwin Smakman, Prof. Paul Koenraad group, Eindhoven University of Technology, The Netherlands. 109

Figure 7.4: (a) Three-dimensional image of one of the APT volumes showing only Sb atoms. Yellow iso-concentration surfaces highlight areas with 9% Sb concentration. (b) – (e) Contour plots of varying Sb concentration composed from a slice through the center of the nanostructures as analyzed by APT. The concentration scale is the same for each plot. A voxel size of 0.5 x 0.5 x 0.5 nm^3 and a delocalization distance of 3 nm were used. Sb concentrations are displayed in color from darker (lower %Sb) to lighter (higher %Sb). Higher concentrations shown in the compact QD in (c) are displayed in white with black contour lines. Note that (d) contains two side-by-side clusters of small islands. (f) and (g) Cross-sectional views along a given *x-z* plane taken from (e). (1), (2), and (3) are described in Figure 5. All scale bars are 5 nm. APT data collected by Prof. Emmanuelle Marquis, MSE Department. 111

Figure 7.5: Line profiles of Sb concentration measured through the center of the nanostructures at locations (1), (2), and (3) in Figure 4(c) and (e) using a cylinder with a diameter of 1.5 nm and a 1.5 nm bin width. The dashed line in each plot is a guide to the eye. 112

Figure 7.6: Current-voltage plots for QD intermediate band solar cells with QDs outside the junction and inside the junction. Figure taken from abstract accepted to the IEEE Photovoltaic Conference 2013.[33] Data measured by Jinyoung Hwang, Prof. Jamie Phillips group, Electrical Engineering Department, University of Michigan. 117

Figure 7.7: External quantum efficiency (EQE) plot showing the enhanced absorption resulting from QDs placed inside the junction. Figure taken from abstract accepted to the IEEE Photovoltaic Conference 2013.[33] Data measured by Jinyoung Hwang, Prof. Jamie Phillips group, Electrical Engineering Department, University of Michigan. 117

Figure 8.1: Atomic force microscope image of InAs QDs grown on lattice matched AlAsSb/InP. 125

Figure 8.2: Photoluminescence spectrum for the InAs QDs on AlAsSb lattice matched to InP. The QD peak is seen at 1.15 eV and the substrate peak is at 1.4 eV. The shoulder on the substrate peak may be the result of the AlAsSb film. 126

Figure 8.3: Omega-2 Theta scans of the InAs QDs on AlAsSb/InP for the (a) (004) and (b) (224) showing a single peak for each. Data collection assisted by Evan Anderson, Prof. Joanna Millunchick group, MSE Department. 126

Abstract

Semiconductor quantum dots are of recent interest for use in various optoelectronic devices such as solar cells, lasers, and quantum computing. For example, embedding quantum dots within an optical nano-cavity is expected to greatly enhance performance of micro-lasers and quantum gates due to their non-linear optical response. For solar cells, quantum dots can be used to create an intermediate energy state within the band gap of the bulk material as originally proposed by Luque and Marti, increasing the thermodynamic efficiency limit to >63%, well beyond that of current devices. These device applications require selecting an appropriate material system, properly preparing the starting growth surface prior to quantum dot growth, and understanding the resulting structural, compositional, and optoelectronic properties of the dots. This work is presented in two parts, each containing multiple related studies on quantum dot nanostructures and the background information necessary for understanding the analysis presented. Part I describes the effects of lateral patterning on the size and composition of InAs quantum dots and advances the current understanding of the effects of lateral separation on dot size and composition. Increasing the pattern spacing results in an increase in quantum dot dimensions, even doubling their size, an increase in wetting layer thickness, and increased dissolution during capping. The In diffusion length during quantum dot nucleation and dissolution upon capping can be determined via patterning to be approximately 0.5 μm and >1.0 μm, respectively. Part II describes the effects of growth conditions and GaAs capping on size, shape, and segregation of Sb in type-II band offset GaSb quantum dots using various analysis

techniques capable of analyzing the morphology, composition, and optical properties of uncapped and buried nanostructures. In particular, three-dimensional analysis of the morphology and composition of buried structures shows that approximately 70% of GaSb dots disintegrate into clusters of small islands with about 1/3 the diameter of their precursor, significantly altering their optoelectronic properties. A detailed analysis of the quantum dot nanostructures is presented in both parts, and examples of devices fabricated through collaborations provide a better understanding of how quantum dots can be properly tailored for specific device applications.

Chapter 1

Introduction and Background

1.1 Introduction

Semiconductor quantum dots (QDs) have become of interest in recent years because of their unique optical and electronic properties, which make them ideal for a variety of device applications such as quantum information processing,[1] lasers,[2,3] and solar cells.[4] The ability to tune the QD band gap by altering the dot size and/or composition makes them advantageous for lasers and telecommunications devices where a specific emission wavelengths are required.[2,3,5] In 1997, Luque and Marti introduced the idea of the intermediate band solar cell[6] in theory,[7] which they later demonstrated[4] using QDs to form the intermediate band. For telecommunications, information processing, and photovoltaic applications, there are a number of fundamental properties of QDs that must be understood prior to device implementation. For example, growth and capping conditions have been shown to affect QD size, areal density, shape, and composition, which, in turn, directly affect their optical and electronic properties. Additionally, the material used for the QDs, the growth surface, and lateral surface patterning prior to dot growth can be used to manipulate dot properties. Understanding the effects of these parameters on dot properties and developing methods for manipulating QD nanostructures to specifically tailor these properties is advantageous for QD devices.

1.2 Objectives and Organization

The goal of this work is to analyze the affects of QD material, surface patterning, surface reconstruction, and capping on QD areal density, size, shape, composition, and their optical and electronic properties. Novel information gained from this work is used to effectively implement QDs in photonic crystals used for quantum information processing and for QD intermediate band solar cells. The broader understanding of QD physics developed here is useful for an array of applications, but these two specific device applications are further developed and devices fabricated through multiple collaborations are briefly presented to demonstrate tangible, real-world examples of the technological advances resulting from this work.

For applications such as QD lasers and quantum information processing, it is advantageous to control dot size, position, and areal density. Dot size directly affects their emission energy, which may need tailored for different applications. For some applications, controlling the QD density and location is critical to device performance. These properties can be controlled using lateral surface patterning, where it is possible to achieve precise placement of an intended number of dots, emitting at a desired energy. Other researchers have used e-beam lithography and focused ion beam (FIB) to demonstrate specific placement of QDs in a controlled manner with good precision.[8-17] The studies presented in this work advance the understanding of the effects of FIB patterning on dot properties by analyzing the effects of patterning parameters on dot dimensions, their optical properties, and QD dissolution upon capping. Photonic crystals containing InAs QDs within the optical cavity were fabricated in collaboration and are briefly discussed.

For solar applications, GaSb/GaAs QDs are studied here because their type-II offset is theorized to be advantageous for increasing charge separation in solar applications.[7] GaSb/GaAs

QD structures have only recently become of interest, and much remains to be understood about the effects of growth conditions and capping on GaSb QD shape and composition. The surface reconstruction of the QD growth surface is known to affect the physical and optical dot properties.[18] Additionally, other researchers have used transmission electron microscopy[19-21] and cross-sectional scanning tunneling microscopy[19,20,22-25] to show significant GaSb QD dissolution upon GaAs capping. This study advances the understanding of GaSb QD growth and capping conditions on dot dimensions and dissolution using various techniques including three-dimensional analysis of buried GaSb nanostructures.

This work is organized into eight chapters describing the necessary background information, the analytical methods used, several studies on QD nanostructures, and proposed future work. The remainder of this chapter introduces the idea of the QD, its growth mechanism and properties. *The goal of this chapter* is to present a basic understanding of QD properties and nucleation and to provide an overview of the ultra-high vacuum equipment used to grow the films and QDs analyzed in each of the studies presented.

Chapter 2: The goal of this chapter is to provide an overview of the primary techniques used to analyze the QD structures. The techniques described in this section include reflective high-energy electron diffraction, focused ion beam surface patterning techniques, atomic force microscopy, atom probe tomography, and photoluminescence. For atom probe tomography, where complex sample preparation is required, a description of the sample preparation method is detailed. Some analytical techniques, which were done by collaborators and/or not used in depth, are not described in this section but their details can be found elsewhere.

1.3 Part I

The goal of Part I is to provide an in depth understanding of the affects of lateral patterning by *in vacuo* focused ion beam on the physical and optoelectronic properties of InAs dots. Part I contains Chapters 3 and 4, which present two studies on focused ion beam patterning of InAs QDs. Ultimately, the findings presented here are used in collaboration with Prof. Vanessa Sih's group in the Physics Department to implement InAs QDs into photonic crystals for quantum information processing. Results from the photonic crystals, which were jointly fabricated with collaborators are briefly discussed.

Chapter 3: The goal of this chapter is to analyze the effects of patterning conditions on QD size and pattern fidelity for multilayer structures with a varying number of QD layers. *The key findings of this chapter* include the effects of patterning conditions on dot size, pattern fidelity, and the effects of increasing the number of layers of QDs. The QD diameter and height are found to increase with the size of the patterned holes and with increased pattern spacing. Pattern fidelity is shown to improve for longer ion beam dwell times, which generally corresponds to larger holes. Increasing the number of QD layers leads to mound formation above the underlying patterned sites, disrupting the pattern fidelity and creating a broadening of the QD photoluminescence. This study also demonstrates the unique ability to use lateral QD patterning to determine the diffusion length of In during QD nucleation for a given set of growth conditions.

Chapter 4: The goal of this chapter is to analyze the effects of patterning on QD dissolution via photoluminescence measurements taken as a function of patterning conditions. *The key findings of this chapter* include analysis of the competing effects of size and dissolution on dot emission energy and a unique ability to distinguish between the In diffusion length on

InAs during dot nucleation and that of In on GaAs during dot dissolution. Quantum dot photoluminescence emission energy is shown to initially decrease with increasing pattern spacing, but then increases for separations greater than 1.0 μm. This shift in photoluminescence emission results from a competition between the effects of dot size and those of dissolution on the dot emission energy.

1.4 Part II

The goal of Part II is to provide an understanding of the effects of growth and capping conditions on the size, shape, and composition of GaSb QDs. Part II contains Chapters 5, 6, and 7, which present studies on GaSb/GaAs QDs, which are of interest for photovoltaic applications because of their type-II band alignment. Ultimately, the findings presented in these chapters are used to effectively implement GaSb QDs into intermediate band solar cells in collaboration with Prof. Jamie Phillips' group in the Electrical Engineering department. Results from the intermediate band solar cells, which were jointly fabricated with collaborators are also briefly discussed.

Chapter 5: The goal of this chapter is to advance the current understanding Sb segregation in both two- to three-dimensional GaSb structures by using atom probe tomography to analyze Sb decay profiles of various nanostrctures. *The key findings of this chapter* include the presence of two different modes of Sb intermixing evident in the Sb decay profiles of quantum well and QD structures. Intermixing in the wetting layer of a QD structure is dominated by surface segregation due to the presence of excess Sb spreading over the wetting layer during dot disintegration upon GaAs capping.

Chapter 6: The goal of this chapter is to analyze the effects of surface reconstruction on QD nucleation and their subsequent physical and optical properties. *The key finding of this*

chapter include the dependence of QD size, areal density, optical properties, and dissolution on the starting surface reconstruction. Dots grown on the Sb-terminated (2x8) surface reconstruction are found to be smaller but have a higher areal density and larger width/height aspect ratio than those grown on the As-terminated (2x4) surface reconstruction. Additionally, they displayed brighter photoluminescence and are more stable under the absence of a group V overpressure.

Chapter 7: The goal of this chapter is to provide detailed, three-dimensional analysis of the shape and composition of buried GaSb QDs using atom probe tomography, which is supplemented by two-dimensional analysis using cross-sectional scanning tunneling microscopy. *The key findings of this chapter* include the dissociation of GaSb QDs into small, ring-like clusters of islands upon capping, which creates a broadening of the dot photoluminescence. These findings are corroborated by 8 band **k.p** calculations of dot transition energies for both compact QDs and dissociated clusters of smaller islands formed during capping.

Chapter 8: The goal of this chapter is to discuss ongoing work and proposed future work. Studies related to capping of GaSb QDs are currently underway, and the results of these studies may be implemented into intermediate band solar cell devices. The goal of these studies is to develop a ways to exploit or eliminate GaSb QD dissolution that occurs during capping. New photovoltaic structures are also being developed with collaborators to power low-energy electronics using room lighting. Finally, work related to a InAs/AlAsSb/InP material system with the intent of fabricating a hot carrier cell is described, and initial data is presented.

1.5 Overview of III-V Semiconductor Quantum Dots

Semiconductor QDs are "zero-dimensional" nanostructures that confine excitons in three dimensions. The term "zero-dimensional" is used to refer to their relatively small dimensions in *x*, *y*, and *z*. Unlike quantum wells, which confine in one dimension, or quantum wires, which

confine in two dimensions, QDs confine excitons in all three dimensions, giving them unique properties and applications. Their small nature and properties have caused some researchers to describe them as "artificial atoms," a comparison which highlights their relatively small number of electrons confined within a relatively small structure with properties that can be altered by the addition of just one electron.[26]

Epitaxially grown semiconductor QD heterostructures are also unique because the difference in lattice constant between the dots and the bulk material creates strain in the QDs, which provides another means of modifying the band gap properties of the heterostructure. For example, the band gap of InAs more than doubles in size for InAs QDs grown on GaAs.[27] The lattice mismatch, size, and composition of the QDs dictate the strain and, subsequently, the optical and electronic properties of the dots as well. These unique properties have made QDs of interest for applications such as lasers, solar cells, and quantum computing.

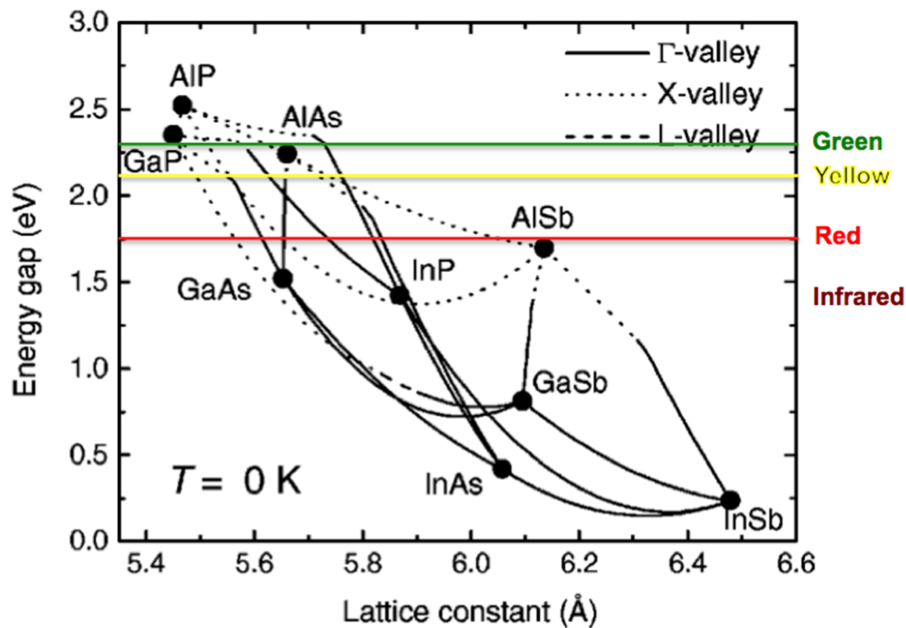

Figure 1.1: Plot of the band gap as a function of lattice parameter. Plot taken from Vurgaftman *et al*.[28] Colored lines added to show approximate ranges of different spectra of visible and infrared light.

The QD nanostructures and thin films described in this work are all III-V materials. These are compounds made up of one element from groups III and one element from group V on the periodic table bonded in a Zinc Blende crystal structure. The primary III-V compounds used for QDs in this study are InAs and GaSb. The primary substrate material used in these studies is GaAs. The band gaps for these materials lie in the infrared regime. Figure 1.1 shows a plot of band gap as a function of lattice parameter for various III-V compounds taken from.[28] Figure 1.2 shows a three-dimensional AFM image of a GaSb/GaAs QD. The dimensions of III-V QDs are generally on the order of 10s of nm in diameter and a few nm in height. The dimensions of the dots are generally controlled by the specific growth parameters used. These parameters include the amount of material deposited for the QDs, the growth temperature, the growth rate, the V/III ratio, the surface reconstruction of the growth surface, and any annealing steps done prior to capping the dots. Some of these growth parameters can also affect the areal density, aspect ratio, and dissolution of dots.

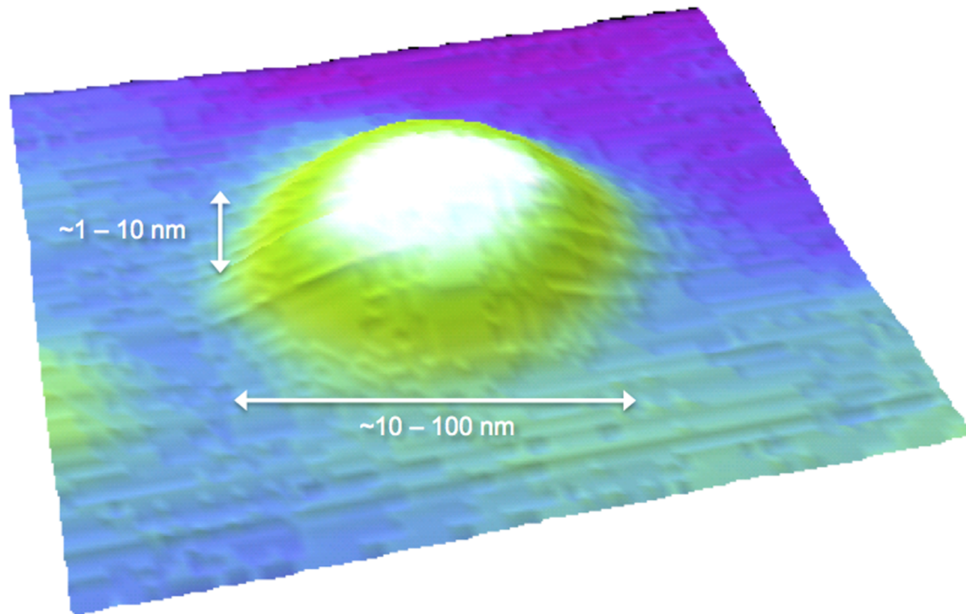

Figure 1.2: Three-dimensional AFM image of a QD showing the general dimensions of self-assembled QDs.

1.6 The Stranski-Krastanov Growth Mode

There are three primary growth modes for epitaxial thin film heterostructures: Frank-van der Merwe, Volmer-Weber, and Stranski-Krastanov. III-V semiconductor QD nucleation most often occurs via the Stranski-Krastanov (SK) growth mode. Figure 1.3 shows a schematic of the SK growth mode. In SK growth, the group III and V materials are deposited simultaneously on the substrate, and a thin, smooth, epitaxial film begins to grow. This thin film is referred to as the wetting layer. The lattice mismatch between the deposited thin film and the substrate creates strain in the film, which increases as the film thickness increases. At some critical film thickness, QDs nucleate to lower the over all energy of the system. The critical thickness for dot nucleation is dependent on the lattice mismatch of the two materials and the specific growth conditions, particularly the growth temperature. During QD nucleation, some material in the wetting layer is consumed to form the dots, but a thin wetting layer remains between the dots.

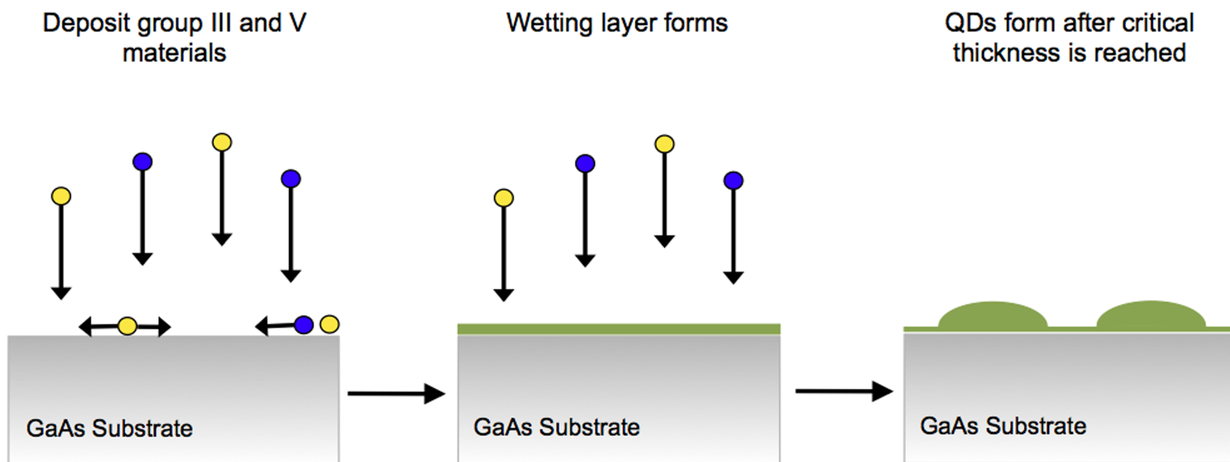

Figure 1.3: A schematic of the main steps of the Stranski-Krastanov growth mode for self-assembled QD nucleation.

1.7 Overview of Molecular Beam Epitaxy

Ultra-high vacuum deposition techniques such as molecular beam epitaxy (MBE) can achieve atomic layer (monolayer) precision for growth of semiconductor thin films. Solid source MBE is an evaporation technique where pure, elemental materials are heated to various temperatures to produce a desired evaporated flux, which is directed toward, and epitaxially deposited onto, a single crystal substrate. The name MBE comes from the evaporated source materials ("molecular beam") and their ordered deposition onto the lattice of the substrate ("epitaxy").[29] Key characteristics of MBE include its ability to precisely control deposition rates with accuracies on the order of 0.01 monolayers per second and film thicknesses at the atomic level.

Thin film growth is done under ultra-high vacuum (10^{-9} – 10^{-11} Torr), which is achieved by using different types of pumps. Two primary types of pumps are used: "capture" pumps and "throughput" pumps. Capture pumps collect atoms or molecules by gettering or implantation (e.g., ion pump, titanium sublimation pump) and freezing (e.g., cryo pump). Throughput pumps (e.g., turbomolecular pump) compress the vacuum gas through a vented outlet where it is removed by a backing pump (i.e., rough pump).[29] In addition to these pumps, liquid nitrogen is filled into a shroud around the vacuum chamber, lowering the pressure up to an order of magnitude as molecules attach to the cold walls on the inside of the chamber. The pressure inside the chamber is monitored using an ion gauge.

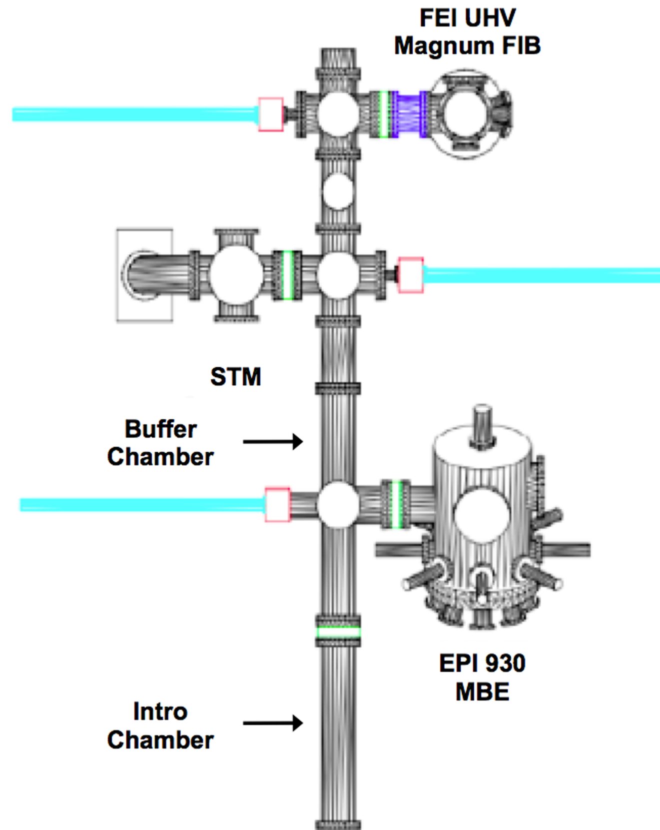

Figure 1.4: A schematic of the lab equipment used in these studies. The MBE chamber is connected *in vacuo* to the scanning tunneling microscope and the FIB. Image used with permission from Dr. Kevin Grossklaus.

The MBE used in these studies is an EPI 930 solid source MBE. The system is comprised of an intro chamber, buffer chamber, and growth chamber (i.e., the MBE chamber) and has a scanning tunneling microscope and focused ion beam connected *in vacuo* via the buffer chamber. Figure 1.4 shows a schematic of the system, and Figure 1.5 shows a photograph of the MBE chamber where each of the cells, which contain the source materials, can be seen. The source materials consist of three group III materials (Ga, In, Al), three group V materials (As, Sb, Bi) and two dopant materials (Si, Be). All cells are oriented directly toward the substrate manipulator where the sample is secured on a molybdenum puck. Figure 1.6 is a schematic of the MBE system showing the primary cells used for these studies. The group III materials, dopants, and Bi

are heated in pyrolytic boron nitride crucibles inside effusion cells, which are heated to a given temperature to achieve a desired flux. Pneumatic shutters are used for these cells to control which material(s) are deposited on the sample. For example, simultaneously opening the Ga and As shutters will result in deposition of a GaAs film where the growth rate is dependent on the flux of the group III material. The As and Sb sources are held at a constant temperature, and their fluxes are controlled using valved crackers. Their cracking zones have separate heating elements from the bulk material, providing a means of differentiating the type of molecule (i.e., As_2 vs. As_4, Sb_2 vs. Sb_4) by adjusting the cracking zone temperature to crack the molecules into the desired form.

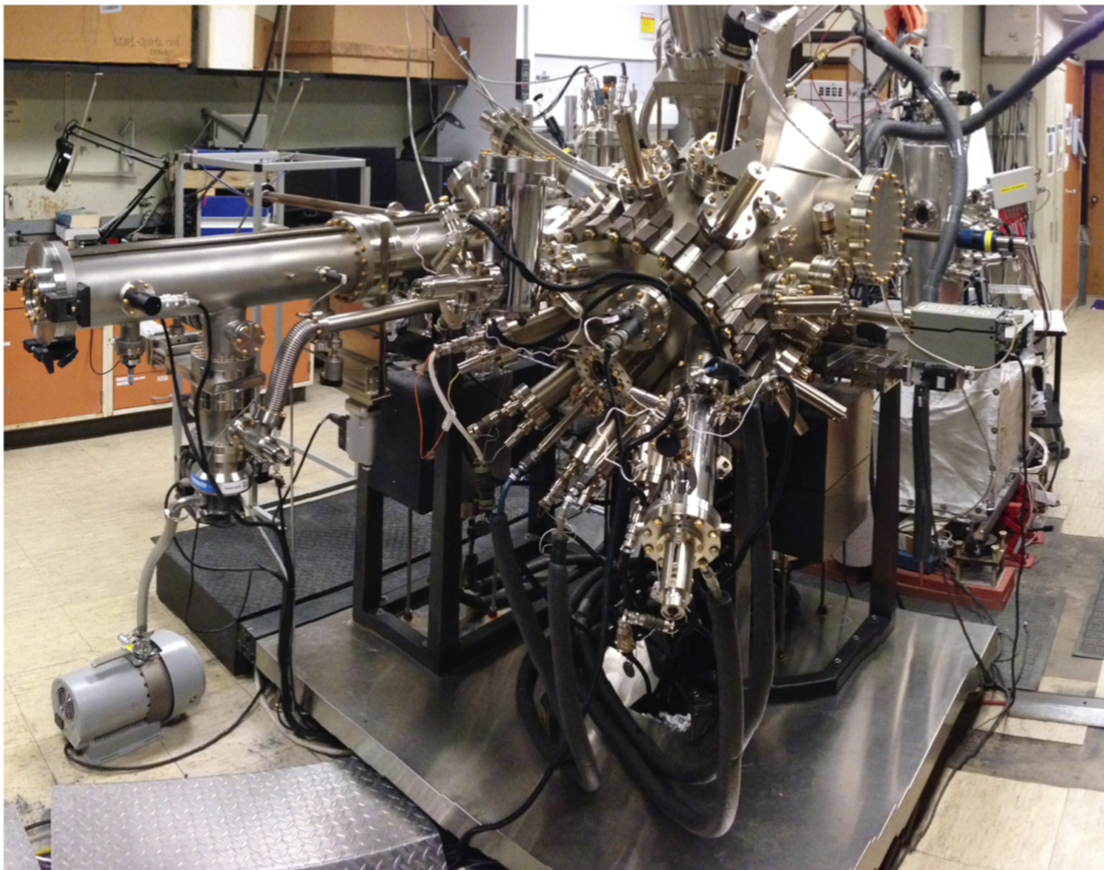

Figure 1.5: A photograph of the MBE used for all film and QD growths in these studies.

Material fluxes are determined using a beam flux monitor (BFM) and rate oscillations. The BFM uses an ion gauge to determine the background pressure of a given material, which can be related to a specific deposition rate in monolayers per second as measured by rate oscillations. Rate oscillations use reflective high-energy electron diffraction to monitor changes in the roughness of the topmost atomic layers and use that information to determine growth rates with atomic precision. The substrate temperature is monitored by an optical pyrometer, which measures blackbody radiation from the hot sample to determine temperature. The optical pyrometer is calibrated against the change in surface reconstruction of GaAs from the c(4x4) to the (2x4) reconstruction at a known temperature of 500 ^{o}C.[29]

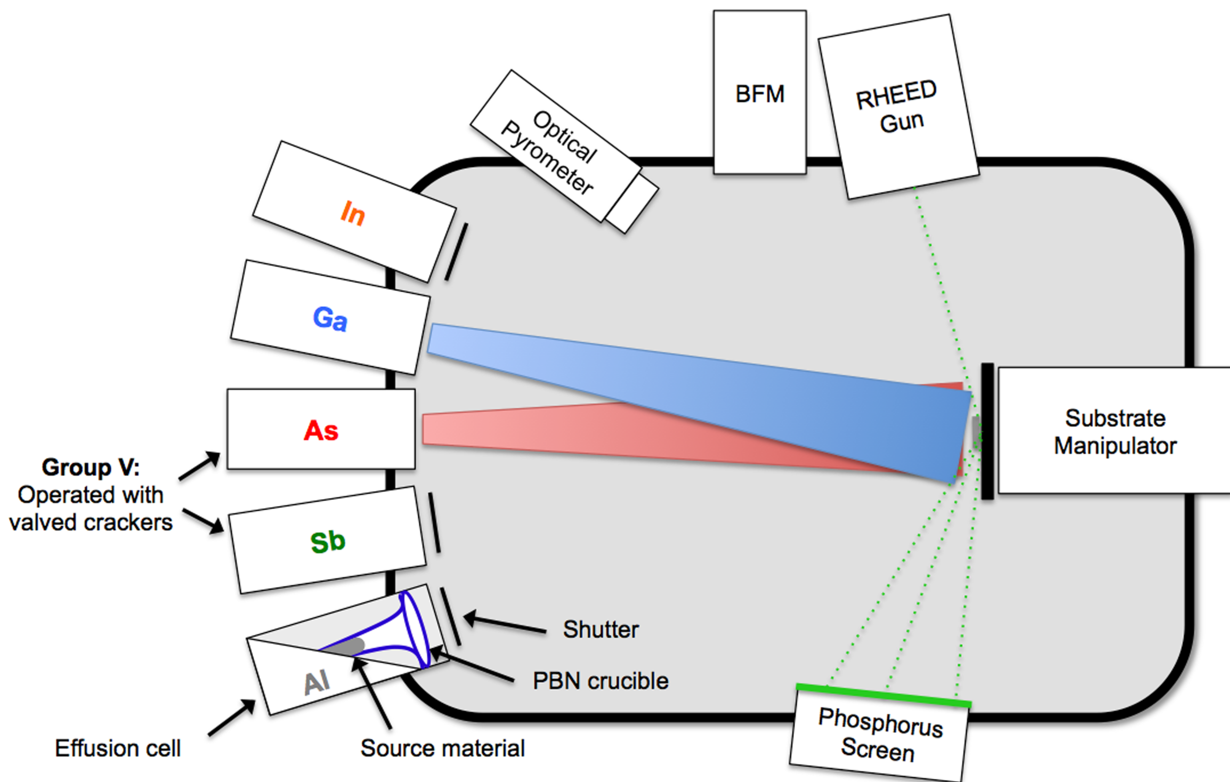

Figure 1.6: Schematic of the MBE chamber used in these studies. The main cells used are shown with the exception of dopant cells.

1.8 References

[1] J. Lee, T. W. Saucer, A. J. Martin, J. Millunchick, and V. Sih, Phys. Rev. Lett. 110, 013602 (2013).

[2] N. N. Ledentsov, V. A. Shchukin, M. Grundmann, N. Kirstaedter, J. Bohrer, O. Schmidt, D. Bimberg, V. M. Ustinov, A. Y. Egorov, A. E. Zhukov, P. S. Kop'ev, S. V. Zaitsev, N. Y. Gordeev, Z. I. Alferov, A. I. Borovkov, A. O. Kosogov, S. S. Ruvimov, P. Werner, U. Gosele, and J. Heydenreich *Phys. Rev. B* **54** 12 8743-8750 (1996).

[3] L. Bouzaiene, B. Ilahi, L. Sfaxi, F. Hassen, H. Maaref, O. Marty, and J. Dazord *Appl. Phys. A* **79** 587-591 (2004).

[4] A. Marti, N. Lopez, E. Antolin, E. Canovas, C. Stanley, C. Farmer, L. Cuadra, and A. Luque, Thin Solid Films **511-512**, 638-644 (2006).

[5] V. Celibert, E. Tranvouez, G. Guillot, C. Bru-Chevallier, L. Grenouillet, P. Duvaut, P. Gilet, P. Ballet, and A. Million *J. of Cryst. Grth. 275 e2313-e2319* (2005).

[6] A. Luque, and A. Marti *Physical Review Lett.* **78** 26 5014 (1997).

[7] L. Cuadra, A. Marti, and A. Luque, Physica E **14**, 162-165 (2002).

[8] H. McKay, P. Rudzinski, A. Dehne, and J. M. Millunchick *Nanotechnology* **18** No. 455303 (2007).

[9] P. Atkinson, O. G. Schmidt, S. P. Bremner, and D. A. Ritchie, *C.R. Physique* **9** 788-803 (2008).

[10] Y. Nakamura, O. G. Schmidt, N. Y. Jin-Phillip, S. Kiravittaya, C. Muller, K. Eberl, H. Grabeldinger, and H. Schweizer *Journal of Crys. Growth* **242** 339-34 (2002).

[11] J. Y. Lee, M. J. Noordhoek, P. Smereka, H. McKay, and J. M. Millunchick *Nanotechnology* **20** No. 285305 (2009).

[12] J. Lee, T. W. Saucer, A. J. Martin, D. Tien, J. M. Millunchick, and V. Sih *Nano Lett.* **11** 1040-1043 (2011).

[13] M. Mehta, D. Reuter, A. Melnikov, A. D. Wieck, and A. Remhof *App. Phys. Lett.* **91** 123108 (2007).

[14] M. Mehta, D. Reuter, A. Melnikov, A. D. Wieck, and A. Remhof *Physica E* **40** 2034-2036 (2008).

[15] S. Kiravittaya, M. Benyoucef, R. Zapf-Gottwick, A. Rastelli, and O. G. Schmidt *Appl. Phys. Lett*. **89** 233102–233104 (2006).

[16] S. Kiravittaya, H. Heidemeyer, and O. G. Schmidt *Physica E* **23** 253-259 (2004).

[17] T. W. Saucer, J. Lee, A. J. Martin, D. Tien, J. M. Millunchick, and V. Sih *Solid State Commun*. **151** 269–271 (2011).

[18] G. Balakrishnan, J. Tatebayashi, A. Khoshakhlagh, S. H. Huang, A. Jallipalli, L. R. Dawson, and D. L. Huffaker, Appl. Phys. Lett. **89**, 161104 (2006).

[19] M. A. Kamarudin, M. Hayne, R. J. Yound, Q. D. Zhuang, T. Ben, and S. I. Molina, Phys. Rev. B 83, 115311 (2011).

[20] R. J. Young, E. P. Smakman, A. M. Sanchez, P. Hodgson, P. M. Koenraad, and M. Hayne, Appl. Phys. Lett. 100, 082104 (2012).

[21] J. Tatebayashi, B. L. Liang, R. B. Laghumavarapu, D. A. Bussian, H. Htoon, V. Klimov, G. Balakrishnan, L. R. Dawson, and D. L. Huffaker, Nanotechnology **19** 295704 (2008).

[22] R. Timm, H. Eisele, A. Lenz, L. Ivanova, G. Balakrishnan, D. L. Huffaker, and M. Dahne, Phys. Rev. Lett. 101, 256101 (2008).

[23] R. Timm, A. Lenz, H. Eisele, L. Ivanova, G. Balakrishnan, D.L. Huffaker, I. Farrer, D. A. Ritchie, and M. Dahne, J. of Vac. Sci. & Tech. *B* 26(4), 1492 (2008).

[24] R. Timm, H. Eisele, A. Lenz, L. Ivanova, V. Vosseburger, T. Warming, D. Bimberg, I. Farrer, D. A. Ritchie, and M. Dahne, Nano Lett. 10, 3972 (2010).

[25] E. P. Smakman, J. K. Garleff, R. J. Young, M. Hayne, P. Rambabu, and P. M. Koenraad, Appl. Phys. Lett. 100, 142116 (2012).

[26] E. Borovitskaya and M. S. Shur, *Quantum Dots*, World Scientific, Rivers Edge, NJ (2002).

[27] C. E. Pryor and M.-E. Pistol *Phys. Rev. B* **72** 205311 (2005).

[28] I. Vurgaftman, J. R. Meyer, and L. R. Ram-Mohan, *J. of Appl. Phys.* **89**(11) (2001) 5815.

[29] R. F. C. Farrow (ed.), *Molecular Beam Epitaxy: Applications to Key Materials*, Noyes Publications, Park Ridge, NJ (1995).

Chapter 2

Introduction to Experimental and Analytical Techniques

Many different analytical techniques were employed during this study in order to better understand QD nucleation, buried and uncapped structure and composition, and optoelectronic QD properties. These analytical techniques include electron diffraction, atomic force microscopy, ion beam patterning, analysis of buried nanostructures via multiple techniques, and photoluminescence of bulk structures and individual QDs. The following sections provide detailed information about the key principles of each technique as well as how they were implemented in this study.

2.1 Reflective High-Energy Electron Diffraction

Reflective high-energy electron diffraction (RHEED) was used to determine growth rates, surface reconstructions and critical thickness for QD nucleation. RHEED is an electron diffraction technique that provides information about atomic bonding and arrangement of surface atoms. For the experiments in this study, a Staib Instruments RHEED system was used and a K-space Associates, Inc., kSA 400 RHEED analysis camera and software were used for rate oscillations. The RHEED gun was operated at 15 kV and 1.5 mA. The incident angle of the collimated electron beam is only a few degrees, allowing it to interact with only the top few monolayers of the film. The diffracted and specular beams strike a phosphorus screen, which fluoresces where the electrons impact it. This creates a diffraction pattern on the screen, which is

imaged by a camera. RHEED provides information about the smoothness of the film, the surface reconstruction, and can be used to determine the critical thickness for QD nucleation.

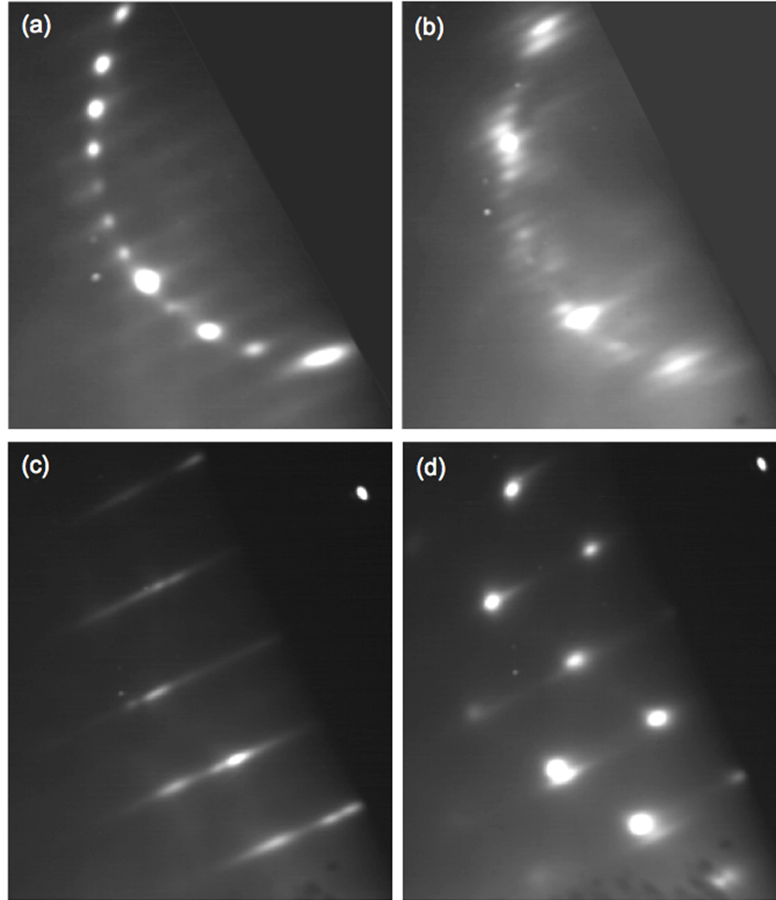

Figure 2.1: RHEED images for (a) the x4 side of the As-terminated (2 x 4) surface reconstruction, (b) the x8 side of the Sb-terminated (2x8) surface reconstruction, (c) the 2x side of a smooth GaAs (2 x 4) surface reconstruction, and (d) a spotty reconstruction formed as a result of QD nucleation.

For GaSb QD growth, RHEED was used to determine the starting surface reconstruction prior to QD growth. Figure 2.1 (a) and (b) show the x4 periodicity of the As-terminated (2 x 4) surface reconstruction and the x8 periodicity of the Sb-terminated (2 x 8) surface reconstruction, respectively. RHEED was also used to determine the point of QD nucleation. Figure 2.1 (c) and (d) show RHEED patterns from a film prior to and after QD nucleation, respectively. A smooth

film results in a streaky diffraction pattern. As a film roughens, it becomes less streaky, and when QDs nucleate, the diffraction pattern becomes spotty like the diffraction pattern shown in Figure 2.1 (d) as a result of electron diffraction off of the rougher surface features, in this case due to the QDs.

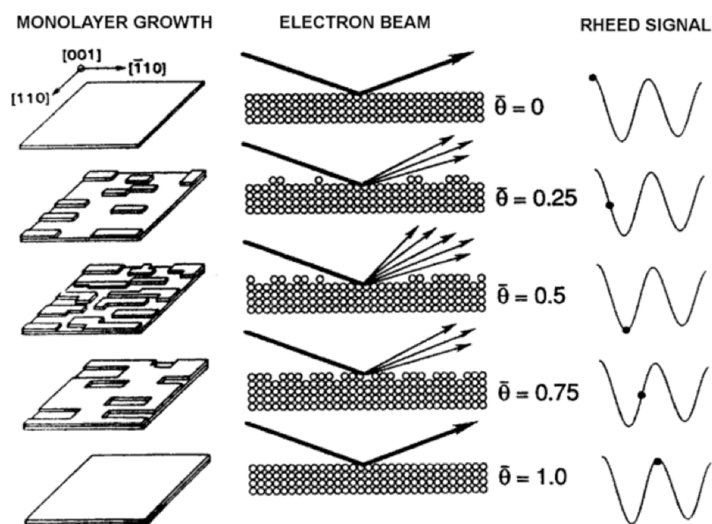

Figure 2.2: A schematic showing the changes in surface roughness and corresponding specular spot intensity during RHEED oscillations. Image adapted from Neave *et al.* and Ohring.[1,2]

Growth rates for all films were measured via rate oscillations. Rate oscillations were done prior to all sample growths. During rate oscillations, a camera is used to monitor the fluorescent intensity of the specular spot during film growth. Figure 2.2 is a schematic showing the oscillation in intensity of the specular spot as each new monolayer of materials is grown.[1,2] Each oscillation peak represents a new monolayer of deposited film. The time between oscillation peaks is used to calculate the growth rate in monolayers per second. Rates for group III elements are measured by depositing the intended element under a group V overpressure while monitoring the intensity of the specular spot. Group V growth rates are measured via "up-take" oscillations where a group III element is initially deposited under no group V overpressure. The film is then,

once again, exposed to the group V element alone, and the specular spot intensity oscillates as the group V element is incorporated into the excess of group III on the film surface.

2.2 Focused Ion Beam Lateral Surface Patterning

The focused ion beam (FIB) is both an imaging and surface modification tool. Imaging with a FIB is similar to imaging with a scanning electron microscope (SEM) except that a FIB uses a focused beam of ions instead of electrons. The fact that a FIB uses ions makes it capable of surface modification due to the mass of the ions, which is significant enough to sputter atoms from the sample surface at a rate dependent on the voltage and current settings of the FIB and the bond strength of the material exposed to the ion beam. The FIB used in these studies is an FEI Company Magnum ion column connected *in vacuo* to the MBE chamber. Figure 2.3 is a schematic of the FIB column. The FIB column consists of the Ga liquid metal ion source (LMIS), which supplies the Ga for the ion beam, a series of high voltage sources, which extract, accelerate, and adjust the current of Ga^+ ions, an aperture strip, which determines the beam size, and a series of magnetic plates, which focus and direct the ion beam. A Ga source is commonly used because of its low melting point (29.8 ^{o}C) and heavy mass, which provides high sputtering rates. The LMIS consists of a Ga reservoir connected to a tungsten tip. The Ga wets the tungsten tip and the high voltages applied to it create a Taylor cone at the tungsten tip from which a controlled current of Ga^+ ions is emitted. Typical ion beam energies range from ~1 keV to 10s of keV,[3] and typical beam currents range from 1 pA to 10s of nA. The FIB used for this study has a resolution limit of ~5 nm.

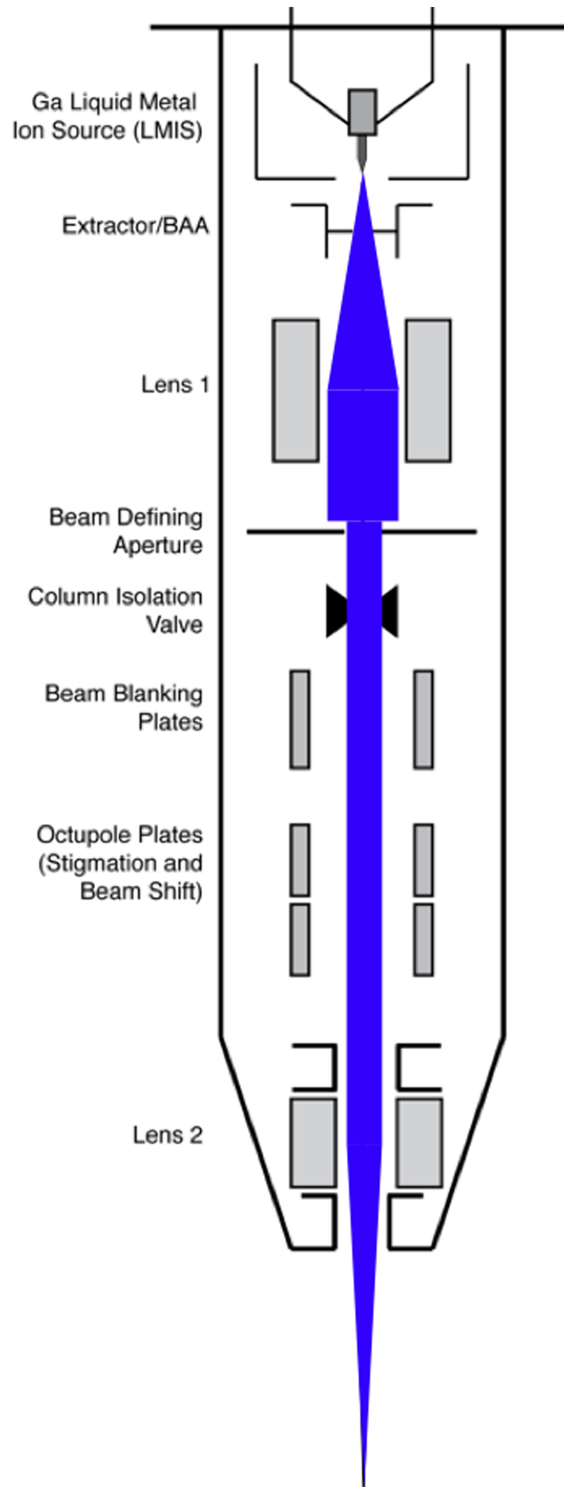

Figure 2.3: A schematic of the Magnum FIB column used for patterning of InAs QDs. The source, lenses, aperture, and octupole plates are indicated. Image courtesy of Dr. Kevin Grossklaus.

The FIB was used to laterally pattern square arrays of small holes in GaAs substrates for directed growth of InAs QDs, which nucleate at the FIB-milled holes below the critical thickness for dot nucleation on a planar surface and, therefore, do not nucleate on the planar regions between and away from the patterned holes. The holes were milled with a single pass of a 30 kV, 10 pA Ga^+ ion beam. Figure 2.4 shows an atomic force microscopy image of a laterally patterned GaAs substrate consisting of a square array of small holes at a predetermined spacing. Stream files are used to make the patterns, which can be simple or complex. The size of the patterned area is limited by the maximum field of view, which is on the order of 750 μm.

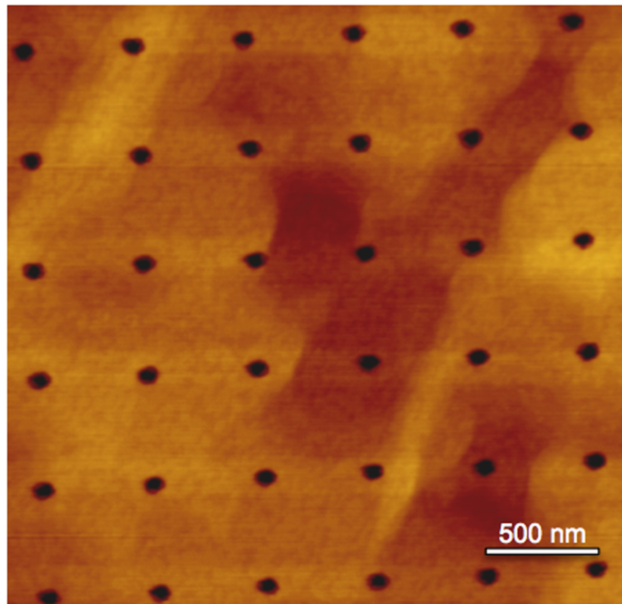

Figure 2.4: Atomic force microscopy image of a square array of FIB-patterned holes prior to InAs QD nucleation on the patterned sites.

2.3 Atomic Force Microscopy

Uncapped QDs were analyzed by atomic force microscopy (AFM) to analyze film quality and to measure QD dimensions and areal density. In this study, samples were analyzed using both a Digital Instruments Nanoscope IIIa AFM and a Veeco Dimension Icon AFM. The

Dimension Icon AFM was used to analyze laterally patterned QDs because its camera system and stage controls were better suited for finding small patterned areas on the sample surface and for aligning the AFM tip above these particular patterns. Both instruments were operated in tapping mode for all analysis. Tapping mode AFM is a surface analysis technique that creates three-dimensional topographical maps of the sample surface by physically tapping the surface with a sharp, Si tip at a given frequency and monitoring the response of the tip as it scans the surface. The tip is attached to the end of a stiff, Si cantilever, and a laser is focused on the topside of the cantilever, opposite the tip. The cantilever is oscillated in the z-direction at one of its resonance frequencies and rastered across the sample surface in x-y. The laser is reflected off of the cantilever and impacts a four-quadrant photodiode detector. As the tip interacts with surface features (e.g., step edges, QDs), the reflected laser beam impacts the detector at different locations due to the change in surface topography. The AFM tip position is controlled by piezoelectric actuators, which move the tip in x and y, and its height in the z-direction is controlled by another piezoelectric actuator. Image resolution in x-y is limited by the diameter of the Si tip, but the resolution in the z-direction can be as small as one atomic step edge. Image scan size can be as large as ~50 μm along each side and as small as ~100 nm along each side. For this study, typical scan sizes were between 0.5 – 10 μm.

The Nanoscope Analysis program was used to analyze film roughness and to measure QD and FIB-patterned hole dimensions. QD and hole measurements were done one-by-one, comparing dimensions in the fast growth and scan directions. SPIP software was also used to measure QD dimensions using a watershed technique, which was used to increase repeatability and decrease error introduced in the one-by-one measurements.

2.4 Atom Probe Tomography

2.4.1 Background

In these studies, atom probe tomography (APT) was used to analyze the composition and shape change of GaSb QDs after GaAs capping and the process of QD nucleation. A Cameca LEAP 4000X was used for the experiments described in these studies. APT is a destructive analytical technique that provides three-dimensional compositional and coordinate information about atoms and molecules within a buried nanostructure. Sample preparation for APT was done using a standard lift-out technique where the sample is attached to a doped Si post on a doped Si substrate. APT data collection is done in ultra-high vacuum at temperatures on the order of 10 – 100 K. APT relies on the concept of charge concentration at a sharp tip to evaporate ions from the surface of the sample using a constant electric field and either an additional pulsed field or pulsed laser. The sample is milled into a sharp, pencil-shaped tip using a FIB and acts as one of the electrodes within the system. The tip has a base diameter of approximately 1 μm and a tip diameter of approximately 100 nm. A hollow, metal electrode, called the local electrode, acts as the second electrode within the system.

Figure 2.5 is a schematic of the LEAP system. Data is collected in either laser voltage or laser pulsing modes. In both modes, a constant voltage on the order of 2 – 20 kV is applied to the sharpened tip. In laser pulsing mode, a laser is focused on the sample tip and pulsed at a desired frequency and energy. In voltage pulsing mode, an additional voltage is pulsed at a given frequency at approximately 10 – 20% of the value of the constant voltage. Samples analyzed in this paper used both voltage and laser pulsing modes. Voltage pulsing mode has been reported to work better for GaSb QDs in GaAs.[4] However, laser pulsing mode was shown to evaporate a higher number of atomic species as opposed to molecules for wetting layer samples. The desired

ion detection rate is set in the LEAP software and the computer increases the constant voltage in a manner such that the chosen ion detection rate is held constant. The detection rate is the rate at which evaporated ions hit the detector. The goal is to evaporate one ion with each pulse, which allows for accurate interpretation of the mass and time of flight of the ion. This provides the information necessary to reconstruct the three-dimensional position of the ion within the bulk nanostructure and to identify the type of ion. The LEAP 4000X uses a reflectron as shown in Figure 2.5 to increase the length of the flight path, which increases accuracy in determining the specific ion.[5] However, the use of a reflectron decreases the number of ions collected by the detector.

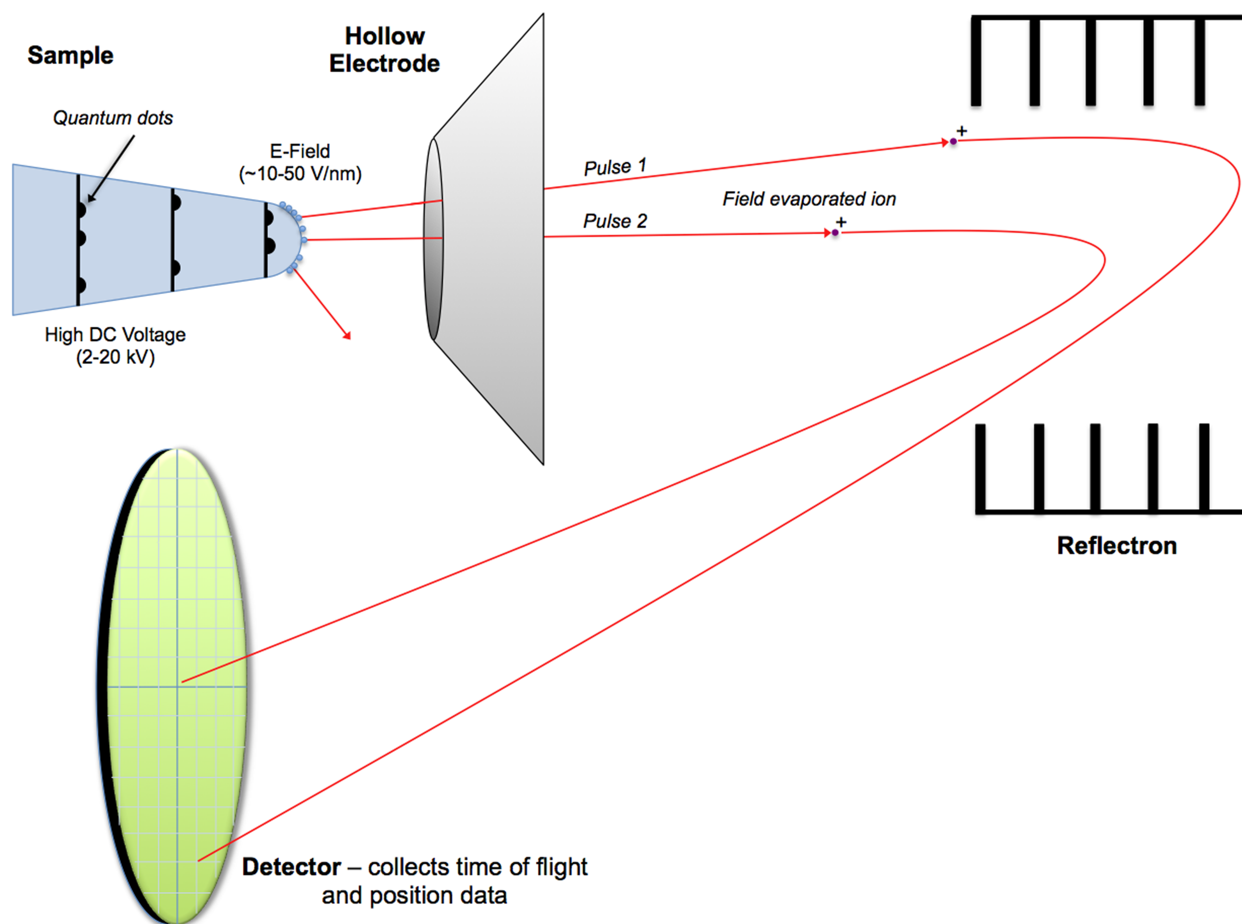

Figure 2.5: A schematic of the Cameca LEAP 4000X atom probe used in these studies showing the sample tip, local electrode, reflectron and detector.

2.4.2 Focused Ion Beam Lift-out

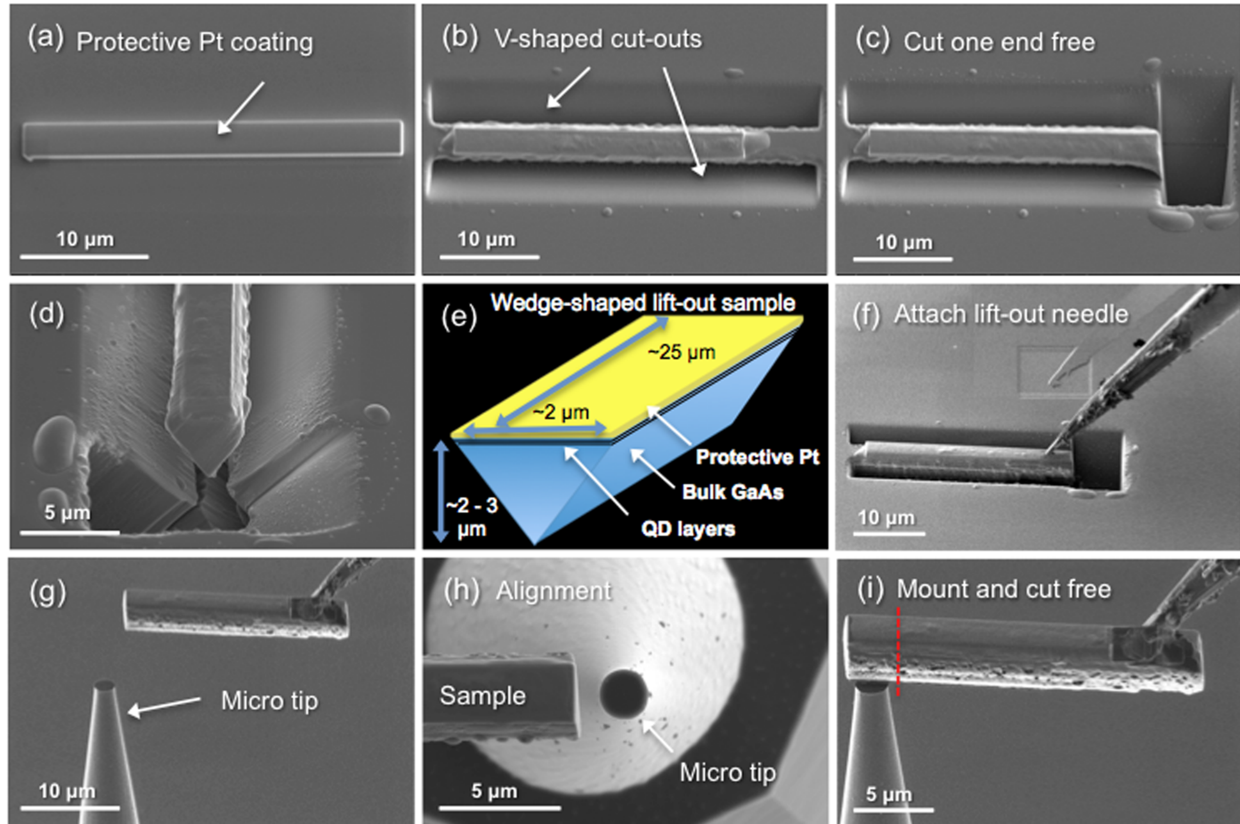

Figure 2.6: Scanning electron microscope and focused ion beam images of (a) – (c) the Pt mask and cut-out steps. (d) End-on view of the "V"-shaped lift-out sample. (e) A schematic of the lift-out specimen showing the approximate dimensions and location of the area of interest with respect to the volume as a whole. (f) – (i) Scanning electron microscopy images of the lift-out process including (f) attaching the needle and lifting it out, (g) and (h) aligning the lift-out sample above the micro-tip, and (i) mounting and cutting each sample volume onto a separate microtip.

APT sample preparation was done in a dual-beam scanning electron microscope (SEM)/FIB using a FIB lift-out technique similar to the method reported by Thompson *et al.*[6] Sample preparation is as much of an art form as a rigid, technical procedure. Therefore, all values (*e.g.*, voltage, current, thickness, width, depth) reported here should be taken as general

guidelines and not an exact procedure. Each sample preparation may be slightly different depending on the material, the number of sharpened tips desired, the purpose of the work being done, the particulars of the sample structure, or the exact SEM/FIB being used and its current working condition. Figure 2.6 shows the key steps required for the surface preparation, FIB lift-out, and attachment to Si microtips, which are the first stages in the APT sample preparation procedure. The key steps in the lift-out process are: 1) Deposition of Pt mask, 2) Milling the undercuts, 3) Attach the lift-out needle, 4) Final cuts and lift-out.

1) Deposition of the Pt mask. A Pt mask is used to protect the area of interest because Pt mills significantly more slowly than GaAs or other III-V materials when exposed to an ion beam. This provides a layer of protection to the area of interest (the QD layers), which is generally very close to the surface. Figure 2.6 (a) shows a SEM image of a Pt mask approximately 25 μm in length and 3 μm wide. Pt deposition can be done using either the ion beam or the electron beam. During Pt deposition, the ion or electron beam rasters over a selected area of the sample as a metal-organic gas containing Pt is released and directed toward the selected area. Basic shapes can be drawn on the screen to designate the area to be coated or more complex bitmaps can be used to make detailed patterns. As the ion or electron beam rasters over the designated area, it cracks the metal-organic molecule causing the Pt to deposit on the surface and its organic counterpart to be pumped out of the chamber. Initial deposition should be done using the electron beam. This is because the ion beam may damage the sample surface prior to depositing the initial atomic layers of Pt. The amount of damage will vary with the current and voltage settings of the ion beam, and may not be overall significant, but using the electron beam guarantees no damage granted that the material is not extremely sensitive to the electron beam. The entire Pt layer or approximately 300 – 500 nm may be deposited using the electron beam, or an initial Pt layer of

100 – 200 nm can be deposited followed by ion beam deposition of the remaining thickness. Increasing the current-to-voltage ratio will increase the rate of electron beam deposition. Typical values for electron beam Pt deposition are an accelerating voltage of 5 kV and current of 1.6 nA. The sample should be tilted to 52° if the ion beam is used for deposition so that the surface is perpendicular to the beam. The Pt mask should be approximately 2 – 3 μm wide and 10 – 30 μm in length, depending on the desired number of APT tips.

2) Milling the undercuts. Undercuts should be made along both long side lengths of the Pt-masked area as shown in Figure 2.6 (b) to produce a “V”-shaped sample. The undercuts should be milled using the ion beam with an accelerating voltage of 30 kV and a current of approximately 0.5 – 5 nA, depending on the milling rate of the material. Higher ion beam currents may tend to produce more re-deposition of Ga and As along the side walls but decrease milling time. Undercuts should be made at a 9° tilt, which places the sample surface at a 43° angle from the ion beam, resulting in the desired “V” shape for the lift-out sample. An Ion beam current of this magnitude (anything greater than 50 pA) should be focused away from the area of interest because a high current ion beam is strong enough to begin milling through the Pt protective layer if the surface is exposed for more than several passes of the ion beam. The beam can be beam-shifted away from the area of interest for focusing and then shifted back prior to milling the undercuts. A mill depth of ~5 – 6 μm is sufficient for the undercuts. After the first undercut is milled, the sample should be rotated 180° prior to making the second undercut in order to properly orient the sample to the FIB column to make the second undercut in the proper direction. After the undercuts are made, one end of the sample can be cut free as shown in Figure 2.6 (c). This cut should be made on the same side from which the tungsten lift-out needle will approach the sample. In some SEM/FIB systems, the tungsten lift-out needle may slightly block

the ion beam from the area of interest when attaching it, making it difficult to cut this end free after attaching the needle. This cut can be made using the same ion beam conditions used for the undercuts, and a mill depth of ~4 – 5 μm is appropriate. The sample should now be suspended from one end like a plank. Figure 2.6 (d) is a SEM image of an end-on view of the lift-out sample showing the "V" shape and size of the lift-out sample. Figure 2.6 (e) is a schematic of the lift-out sample, which more clearly shows the shape, dimensions, and location of the area of interest with the structure.

3) Attach the lift-out needle. The sample stage should not be tilted during lift-out when using the FEI Nova 200 Nanolab SEM/FIB or the FEI Helios 650 Nanolab SEM/FIB in the Electron Micro-beam Analysis Laboratory (EMAL) at the University of Michigan. Because of the 52° offset of the FIB and SEM columns, the two beams can be used to analyze the specific *x*-*y* position of the needle (using the SEM) as well as the *z*-height (using the FIB) as the needle is approaching the sample. An ion beam voltage of 30 kV can be used for imaging during this process, but the current should not be set higher than 30 pA to ensure that no damage is done to the surface or the Pt layer while the lift-out needle is aligned and attached. A tungsten lift-out needle with a sharp tip (~1 μm diameter prior to first use) is slowly brought down above the end of the sample that was cut free. The needle should be brought into contact with the Pt coated part of the sample at a very slow rate of approximately 0.5 – 1.0 μms^{-1}. Figure 2.6 (f) shows a FIB image of the lift-out needle prior to attaching it with Pt.

When the needle comes into contact with the sample, a slight change in contrast will be visible in both the ion beam and the electron beam. A slight flex in the sample may be seen if the needle pushes down too hard on the end of the sample that has been cut free. Once the needle is in contact, it can be attached using ion beam or electron beam Pt deposition. A "regular cross-

section" should be used to deposit the Pt and should cover part of the needle tip and part of the Pt coated sample. A Pt thickness of 200 – 300 nm should be deposited to attach the needle as seen in Figure 2.6 (g). This should provide adequate attachment, however, more Pt can be deposited as needed. More than 500 nm of Pt is unnecessary due to the extremely low mass of the sample.

4) Final cuts and lift-out. After attaching the lift-out needle, the other end of the sample is cut free using an ion beam of 30 kV and 0.5 – 5 nA. Again, the ion beam ought to be focused away from the area of interest. It is imperative that the beam shifts be used to shift the beam away from the area of interest during this step because shifting the sample stage will cause the lift-out needle to break free from the sample and may even destroy the lift-out sample. It is also imperative that the ion beam current is set back to 30 pA after the sample is cut free so that the sample is not unintentionally imaged with the higher current beam. The sample is then slowly lifted up and a trench remains where it once sat.

2.4.3 Atom Probe Tip Milling

The second stage in APT sample prep is attaching the sample to the Si microtips and annularly milling each tip into their final tip shape. The atom probe Si coupon may be placed on carbon or copper tape next to the sample. However, sample drift may be noticed during mounting of the sample onto the Si posts and during annular milling if copper tape is used due to poor adhesion through the tape. Keeping the Si coupon on the copper APT holder while attaching the sample to the Si posts and annularly milling each tip eliminates this problem and any risks involved with transferring the sample from the tape to the copper APT holder. There are also four key steps to this stage of APT sample preparation: 1) Mounting to Si posts, 2) Initial annular milling, 3) Filling of voids, and 4) Final milling steps.

1) Mounting to Si posts. The Si coupon should be aligned within the SEM/FIB such that one row of Si posts runs along the eucentric rotation axis so that the Si coupon can be moved from one Si post to the next without requiring realignment. Figure 2.6 (g) and (h) show one of the Si microtips as the sample and lift-out needle approach. The lift-out needle with the sample attached to it should be slowly brought in above one of the Si microtips at the end of the row. The end of the sample opposite the lift-out needle should be aligned above the first Si microtip as shown in Figure 2.6 (i). The x-y position above the Si microtip and the z-height above it can be determined using the electron and ion beams, respectively, as shown in Figure 2.6 (g) and (h). Again, a slight change in contrast is observed when the sample comes into contact with the Si microtip, and if the sample is brought down too far, it will flex slightly. If the sample flexes, it should be raised back up until it sits level and remains in contact with the Si microtip.

The sample should then be attached to the post using ion beam Pt deposition. The Pt can be deposited via a two-step process where a small area at the contact point is deposited first with a thickness of ~200 nm, followed by a larger area with the same thickness. The Pt weld can also be deposited in one step with a thickness of ~300 – 500 nm. The final Pt weld should look similar that shown in Figure 2.7 (a). The Pt weld does not need to reach the top of the sample. The sample should then be cut off using an ion beam with a current of 0.5 – 5 nA very close to the Si post as shown by the dashed line in Figure 2.6 (i). The lift-out needle should then be raised up and sample stage should be shifted to bring the next Si microtip to the center of the field of view. The above procedure is repeated, and as many samples as desired are attached to the Si microtips in that row. Once the desired number of samples is mounted, the sample stage is rotated 180° to Pt weld the backside of each sample in the same manner that the front side was Pt welded. The samples are now ready for the initial annular milling.

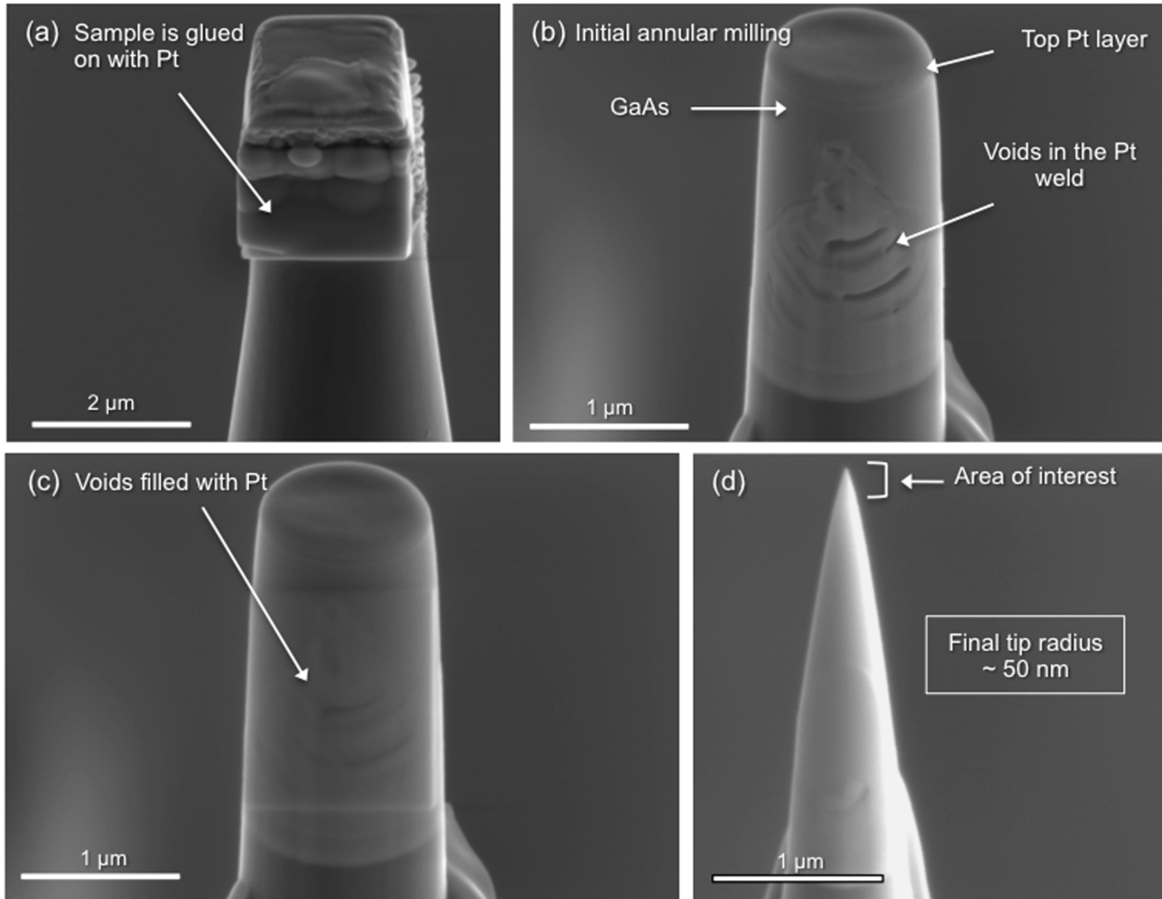

Figure 2.7: Scanning electron microscope images of the tip shaping steps. (a) Initial Pt gluing on both sides of the sample. (b) Initial milling and (c) filling of any voids with Pt. (d) Final tip shaping to achieve a tip radius of ~ 50 nm with the features of interest generally within the first 200 nm from the apex of the tip.

2) Initial annular milling. For annular milling, the sample should be tilted to 52° such that it is perpendicular to the ion beam. All annular milling should be done using the "regular cross-section" circle shape. This milling pattern will be used for all subsequent milling. The outer diameter of the circle should be set to encompass the entire sample (~4 – 6 µm). The inner diameter is initially set to ~1200 – 2000 nm, and the ion beam voltage and current are set to approximately 30 kV and 80 nA in order to decrease the time required for the initial milling step. Depending on the microscope being used, it may be possible to watch the ion beam milling in

live time using the electron beam. A higher electron beam current will generally provide a more clear real-time image during FIB milling. After initial milling, the sample should look similar to the one shown in Figure 2.7 (a).

3) Filling of voids. During the initial milling, voids in the Pt weld may appear as shown in Figure 2.7 (b). Voids are filled in using electron beam Pt deposition because the electron beam is looking at the side of the sample tip. After filling any voids on one side, the sample should be rotated 180° in order to check for voids on the other side. Filling of voids may result in excess Pt as seen in Figure 2.7 (c). In this case, the sample should be milled to remove any bulges in the Pt from the surface.

4) Final milling steps. The final milling is the most complicated step in the APT sample preparation and is often more of an art and developed skill than a rigid procedure. If possible, the final milling steps should be watched in real time using the electron beam. The ion beam should be set to ~20 kV and ~50 pA for the next milling step. It is possible to use the 30 kV ion beam for the entire milling process, but it is more difficult to control the mill depth and achieve the desired tip shape. The outer diameter of the "Circle" pattern should be decreased such that it is just larger than the diameter of the tip (~2000 nm), and the inner diameter should be decreased to approximately 600 – 800 nm. The tip should be milled such that it begins to transition from a cylinder to a cone shape as shown in Figure 2.8 (a) to (b). Milling should be stopped once the narrowed region reaches the bottom of the Pt weld.

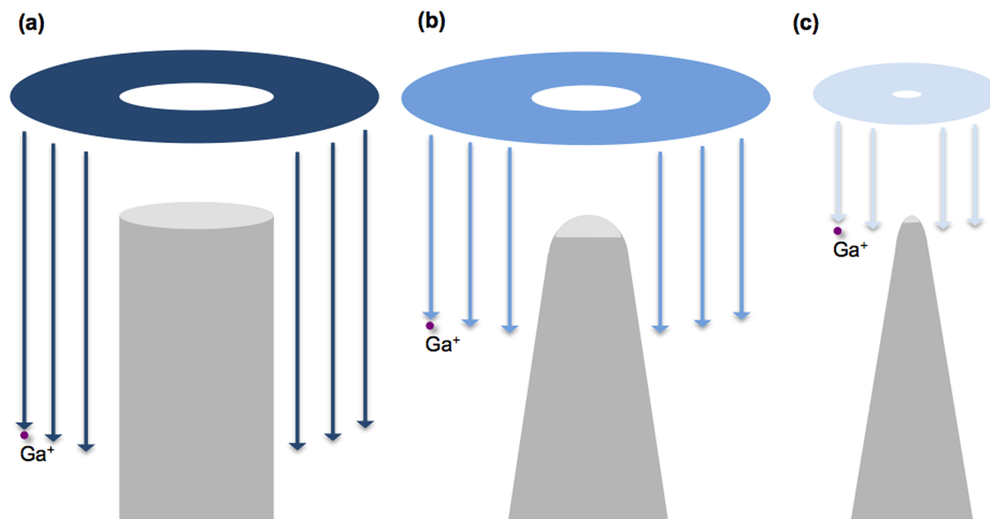

Figure 2.8: A schematic illustrating the milling steps used to create the atom probe tips. Adapted from Gault *et al.*[5]

The next and final milling step can be done using the same type of “Circle” pattern or by using a stream file developed by Dr. Allen Hunter. The ion beam should be set to ~5 kV and ~40 pA for the final tip shaping. The stream files developed for tip milling are circular patterns designed to mill in a spiral shape from the outside in, decreasing the dwell time of the FIB as the beam approaches the apex of the tip. There are several different patterns designed to form tips with varying bevel angles. The pattern are designed to be independent of magnification so the magnification should be selected such that the outer diameter of the pattern is no larger than ~1000 nm (a magnification of ~80 kx is appropriate). The pattern should be monitored in real time or paused after every few passes to verify tip shape and milling rate. The goal is to achieve a tip shape similar to that of Figure 2.8 (c). The final remaining Pt can be removed using the 5 kV or 2 kV ion beam and at the lowest possible current to reduce FIB damage at the area of interest and so to slow the milling rate.

If the “Circle” pattern is used instead of a stream file, the out diameter should be set to approximately 1000nm and the inner diameter slowly decreased to slowly sharpen the tip. If

milling cannot be watched in real time, it is imperative that the milling is stopped frequently to check the progress so that the sample is not destroyed. To form the desired taper, the inner diameter of the milling pattern is decreased in steps of ~100 nm at a time down to 100 nm and the ion beam current is decreased throughout this as necessary. Once the inner diameter reaches approximately ~400 nm, the ion beam voltage can be decreased to ~8 kV. Note that at voltages less than 30 kV the ion beam image may not be very clear. However, it is only necessary that the tip is visible and in relatively good focus. The focus and stigmatism may require adjustment each time the ion beam voltage and/or current are changed. The goal is to achieve a final tip shape similar to the one shown in Figure 2.7 (d). If there is any Pt remaining after the tip diameter reaches ~100 nm, the remaining Pt can be removed using a ion beam voltage of ~5 kV and the smallest possible current. Further milling may be done prior to removing the remaining Pt in order to change the slope of the sides of the tip. Steeper sidewalls will allow the tip to evaporate further down before fracturing because the point of fracture is dependent on the curvature at the evaporation front. However, less steep sidewalls may be better for tips run in laser mode.

2.4.4 Three-dimensional Data Reconstruction and Analysis

The APT data is reconstructed into a three-dimensional image using IVAS analysis software. The two primary parameters that can be altered to adjust the reconstruction are the evaporation field and the image compression factor. The evaporation field should be similar for samples of a given material, and for the data analyzed in this work was set to 35 V. The evaporation field and image compression factor are adjusted to flatten known planar features and to adjust known separation distances to their proper lengths. Once the three-dimensional reconstruction is complete, data can be analyzed by creating iso-concentration surfaces, one-

dimensional concentration profiles through desired volumes and locations within the structure, and by creating composition contour plots from layered iso-concentration surfaces. Figure 2.9 shows examples of three-dimensional APT reconstructions. These include an example of an Sb iso-concentration surface where a surface of a given percent Sb is highlighted in yellow. When creating iso-concentration profiles, a voxel size of 0.5 x 0.5 x 0.5 nm^3 is sufficiently small, and a delocalization distance of 3 nm, which is the standard setting, is fine. A smaller voxel size may be considered to skew the data, particularly when the delocalization distance is very large in comparison. For one-dimensional line profiles, the bin size should not be set below approximately 0.2 nm because this is nominally the size of one of the atoms in the system, and the molecules should always be decomposed by checking the box labeled "decompose" next to the line profile data. This guarantees that ions that come off as molecules (e.g., As_2^{2+}) are counted as two As atoms instead of one when calculating concentrations of a given element.

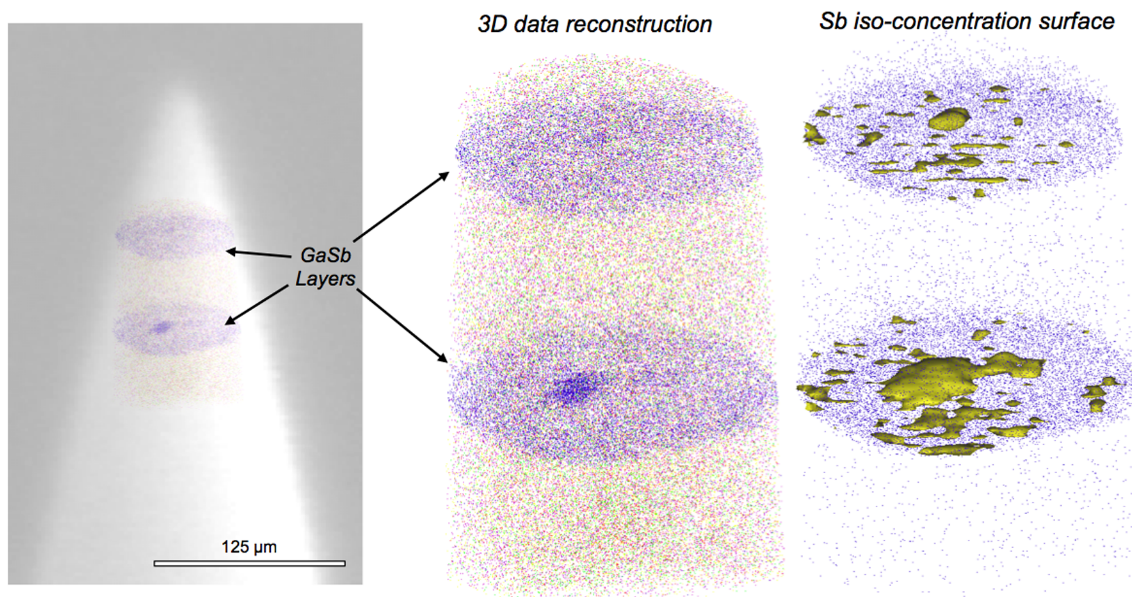

Figure 2.9: Examples of atom probe data reconstructed in three dimensions showing where the data comes from within the sample tip and examples of an iso-concentration surface highlighting a given percent of Sb in yellow.

2.5 Photoluminescence

Samples were analyzed using PL in this study to better understand the effects of growth conditions and substrate patterning on the optoelectronic properties of the varies InAs and GaSb QD nanostructures grown under varying conditions. Photoluminescence (PL) is a process in which high-energy photons from a laser first excite electrons from the valence band to the conduction band of a material. If the electron energy is greater than that of the conduction band level, it relaxes back down to the conduction band edge and releases energy in the form of heat. This is referred to as thermalization loss. The electron is then able to radiatively recombine with a hole in the valence band, which in turn releases a photon with energy equal to the band gap energy. In order to obtain PL emission from each part of the structure, the laser energy must exceed the largest band gap within the structure, which in this study is the ~1.5 eV band gap of GaAs. A laser with a wavelength of 633 nm (~2 eV) was used for all PL measurements. PL measurements were taken at temperatures ranging from 10 K to 300 K using a He flow cryostat to achieve low temperature. Additionally, laser powers ranging from 10s of μW to 100s of μW were also used. Figure 2.10 shows a schematic of the recombination pathways for a GaSb QD, GaSb WL, and GaAs substrate. Both macro- and micro-PL were used to study patterned InAs QDs. Macro-PL was used to analyze the change in QD PL peak energy with changing patterning conditions, and micro-PL was used to optically probe individual QDs with large pattern spacings. Micro-PL was also used to create two-dimensional maps of the emission energy of QDs at each particular patterned site in a given area. GaSb QDs were only analyzed using macro-PL.

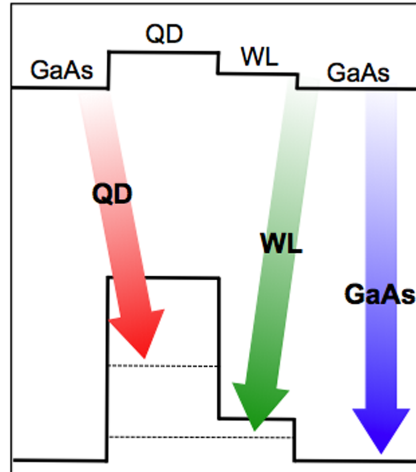

Figure 2.10: A schematic of the recombination pathways of GaSb/GaAs QDs and wetting layer with a type-II band alignment.

2.6 References:

[1] J. H. Neave, B. A. Joyce, P. J. Dobson, and N. Norton, *Appl. Phys. A* **31** 1-8 (1983).

[2] M. Ohring, *The Materials Science of Thin Films,* San Diego: Academic Press, pp. 339-344 (1992).

[3] L. A. Giannuzzi and F. A. Stevie (eds) *Introduction to Focused Ion Beams: Instrumentation, Theory, Techniques, and Practice* (Springer Science+Business Media, Inc., Boston, MA 2005).

[4] A. M. Beltran, E. A. Marquis, A. G. Taboada, J. M. Ripalda, J. M. Garcia, and S. I. Molina, *Ultramicroscopy* 111**,** 1073 (2011).

[5] B. Gault, M. P. Moody, J. M. Cairney, S. P. Ringer, *Atom Probe Microscopy*, Springer 2012, New York, Heidelberg, Dordrecht, London.

[6] K. Thompson, D. Lawrence, D. J. Larson, J. D. Olson, T. F. Kelly, and B. Gorman, *Ultramicroscopy* 107, 131 (2007).

PART I

Analysis of InAs Quantum Dots Patterned by *In Vacuo* Focused Ion Beam

Part I contains Chapters 3 and 4, which present studies on focused ion beam patterned InAs/GaAs QDs that are of particular interest for quantum information processing. *The goal of Part I* is to provide an in depth understanding of the affects of lateral patterning on the physical and optoelectronic properties of InAs QDs. Chapter 3 discusses the effects of patterning conditions on QD dimensions and the pattern fidelity as well as the effects of increasing the total number of QD layers. Chapter 4 provides a detailed analysis of the effects of patterning on QD dissolution as analyzed by photoluminescence. These chapters also discuss the ability to use patterning to determine the diffusion length of In atoms on both InAs and GaAs surfaces. The findings presented here are used in collaboration with Prof. Vanessa Sih's group in the Physics Department with the goal of implementing focused ion beam patterned InAs QDs into photonic crystals for quantum information processing. Results from the photonic crystals, which were jointly fabricated with collaborators are briefly discussed.

Chapter 3

Lateral Patterning of Multilayer InAs/GaAs(001) Quantum Dot Structures by *In Vacuo* Focused Ion Beam

This chapter reports on the effects of patterning and layering on multilayer InAs/GaAs(001) quantum dot structures laterally ordered using an *in vacuo* focused ion beam. Patterned hole size and lateral pattern spacing affected quantum dot size and the fidelity of the quantum dots with respect to the lateral patterns. 100% pattern fidelity was retained after six layers of dots for a 9.0 ms focused ion beam dwell time and 2.0 μm lateral pattern spacing. Analysis of the change in quantum dot size as a function of pattern spacing provided a means of estimating the maximum average adatom surface diffusion length to be approximately 500 nm, and demonstrated the ability to alter the wetting layer thickness via pattern spacing. Increasing the number of layers from six to 26 resulted in mound formation, which destroyed pattern fidelity at close pattern spacings and led to a bimodal quantum dot size distribution as measured by atomic force microscopy. The bimodal size distribution also affected the optical properties of the dots, causing a split quantum dot photoluminescence peak where the separation between the split peaks increased with increasing pattern spacing.

3.1 Introduction

Quantum dots (QD) are of interest for applications such as intermediate band solar cells,[1,2] lasers,[3,4] and quantum computing. For these applications, it is advantageous to control

the QD dimensions and areal density because these properties directly influence the optical and electronic properties of QD structures. Additionally, controlling QD position is beneficial for some quantum computing technologies where coupling QDs to photonic crystal cavities requires precise QD positioning to achieve good spatial and spectral overlap of the QD and cavity mode.[5,6] InAs QDs are typically grown by self-assembly via the Stranski-Krastanov growth mode. When using this growth mode, QD position is random and the size is primarily controlled by the growth temperature, deposition rate, and the amount of material deposited. Preferential QD nucleation can be achieved by altering surface morphology in specific areas, providing a means of controlling dot placement. InAs/GaAs QDs have been shown to preferentially nucleate on focused ion beam (FIB) irradiated surfaces prior to reaching the critical thickness for nucleation on non-irradiated surfaces.[7] Furthermore, lateral ordering of QDs has been demonstrated on pre-patterned arrays of holes via methods such as *ex vacuo* e-beam lithography[8,9] and *in vacuo* FIB patterning for Ge/Si QDs[10-12] and InAs/GaAs QDs.[13-16] Macro- and micro-photoluminescence have been measured from lithographically-patterned[17] and FIB-patterned[15,19] InAs/GaAs QDs. Additionally, single QD emission with a line width of 160 μeV has been measured from FIB-patterned QDs.[14]

Directed growth techniques are valuable because lateral patterning provides better control over QD density and position.[14,18,19] *Ex vacuo* patterning techniques require exposure to air between patterning and QD growth, resulting in the formation of an oxide layer, which must be removed prior to QD growth and can negatively affect the optical properties of the dots.[20] In contrast, *in vacuo* FIB patterning can be used to produce laterally ordered QDs while keeping the sample within the protective confines of the vacuum at all times. Previous work has demonstrated the effects of FIB patterning conditions on single layers of QDs[13,15,16] and on the

optical properties of multilayer FIB-patterned QD structures.[15,19] This chapter demonstrates the effects of *in vacuo* FIB patterning on QD diameter, density, pattern fidelity, and optical properties as well as the effect of increased layering on surface morphology for multilayer InAs/GaAs QD structures. This chapter also demonstrates FIB patterning as a method for estimating the maximum adatom diffusion length for a given set of growth conditions and as a means of altering the wetting layer thickness.

3.2 Experimental Procedure

Two multilayer InAs/GaAs(001) QD structures were grown by molecular beam epitaxy (MBE) on FIB-patterned GaAs(001) substrates. Figure 3.1 is a schematic of the multilayer structures grown. A 500 nm GaAs buffer layer was grown on both samples at T = 590 ^{o}C. Following buffer growth, the samples were transferred *in vacuo* to the focused ion beam (FIB) for patterning of 40 x 40 μm^2 arrays of holes. The holes were FIB-milled with a single pass of a 10 pA, 30 keV Ga^+ focused ion beam. FIB dwell times were 1.0, 3.0, 6.0, and 9.0 ms, each at pattern spacings of 0.25, 0.5, 1.0, and 2.0 μm, for a total of 16 different patterns. The FIB dwell time determined the dimensions of the FIB-milled holes. After patterning, the samples were transferred *in vacuo* back to the MBE for QD growth. 2.0 monolayers (ML) of InAs was deposited at T = 485 ^{o}C for the QDs at a rate of 0.11 MLs^{-1} and immediately capped with GaAs at a rate of 1.0 MLs^{-1}. The QD growth and GaAs capping process was repeated, creating multilayer structures with six and 26 layers. The spacer layer thickness was 20 nm for the six layer sample and 18 nm for the 26 layer sample. The topmost layer of QDs remained uncapped for both samples for analysis by atomic force microscopy (AFM).

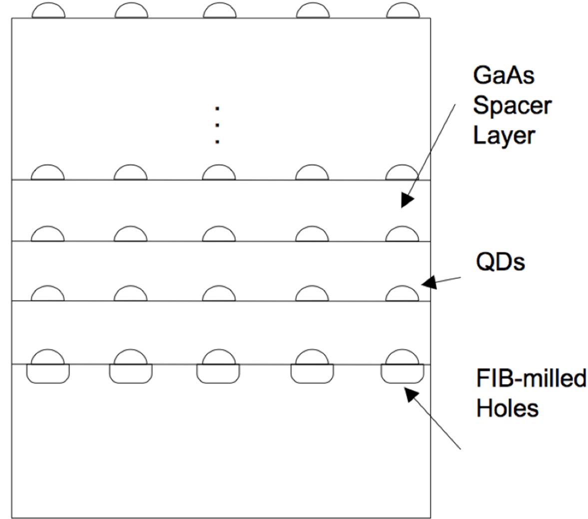

Figure 3.1: A schematic of the FIB-patterned six and 26 layer InAs/GaAs QD structures. Square arrays of FIB-milled holes were patterned at the substrate with pattern spacings of 0.25, 0.5, 1.0, and 2.0 μm each at FIB dwell times of 1.0, 3.0, 6.0, and 9.0 ms. 2.0 ML of InAs was deposited for the QDs for both samples. The GaAs spacer layer thicknesses were 20 and 18 nm for the six and 26 layer samples, respectively.

3.3 Data Analysis

3.3.1 Effects of FIB Dwell Time on QD Dimensions and Pattern Fidelity

For the six layer sample, QDs on the uncapped surface nucleated only in the patterned areas and only above the patterned sites due to the formation of preferential nucleation sites created at the initial layer by the FIB.[7,13,14,19] The holes were milled only at the substrate for both samples (See Figure 3.1). The dimensions of the FIB-milled holes were measured on a separate sample. Hole dimensions increased linearly in size from 85 ± 9 nm in diameter and 3.0 ± 0.3 nm in depth for a 1.0 ms FIB dwell time to 133 ± 14 nm in diameter and 12 ± 1 nm in depth for a 9.0 ms FIB dwell time. Figure 3.2 (a) and (b) show plots of the hole dimensions as a function of FIB dwell time for a 2.0 μm pattern spacing. Figure 3.3 shows AFM images of the uncapped sixth

layer for the 1.0, 3.0, 6.0, and 9.0 ms FIB dwell time patterns each at a pattern spacing of 2.0 µm. QDs at the sixth layer were aligned above the underlying FIB-milled holes. All areas away from the holes are devoid of QDs because the deposited InAs thickness was below the critical thickness for QD nucleation on a planar surface for the given growth conditions. Figure 3.2 (a) and (b) also show plots of the QD dimensions at the sixth layer as a function of FIB dwell time for a 2.0 µm pattern spacing. All QD measurements were performed by a watershed technique, which employed a slope percent to determine a baseline for measuring QD diameter and height. The QDs increased in size with increasing FIB dwell time from 47 ± 12 nm in diameter and 5 ± 2 nm in height for the 1.0 ms FIB dwell time to 91 ± 28 nm in diameter and 15 ± 8 nm in height for the 9.0 ms FIB dwell time. The difference in size between the QDs on the longer and shorter FIB dwell time patterns may be due to a tendency for multi-dot nucleation on the shorter two FIB dwell time patterns (Figure 3.2 (c) and inset in Figure 3.3 (a)). For the 1.0 and 3.0 ms FIB dwell time patterns, the FIB-milled holes at the substrate were smaller and shallower, thus more likely to fill during GaAs capping and layering than the larger, deeper holes milled by the 6.0 and 9.0 ms FIB dwell times. Complete or partial filling of the smaller holes resulted in a smoother surface where either no QDs formed or multiple dots formed at a single patterned site due to the step edge density at those locations. In contrast, the steep sidewalls of the partially filled holes milled by the longer FIB dwell times forced the InAs down toward the bottom of the holes, forming a single QD as shown in the inset in Figure 3.3 (d). Kinetic Monte Carlo simulations by Lee *et al.* demonstrate these same principles for InAs QD formation on FIB-patterned GaAs, resulting in QD nucleation at the bottom of the FIB-milled hole when the sidewalls were steep.[13]

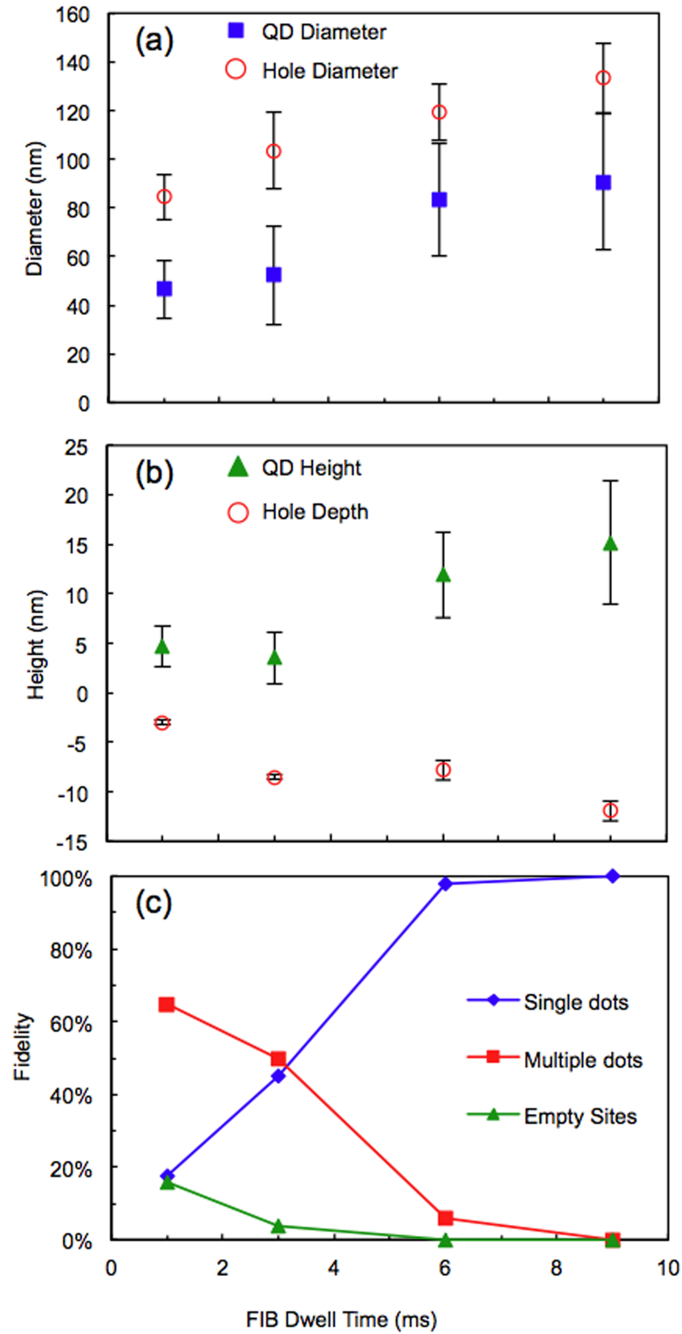

Figure 3.2: Plots of (a) QD diameter as measured at the sixth layer and FIB-milled hole diameter as measured at the substrate of a separate sample; (b) QD height as measured at the sixth layer and FIB-milled hole depth as measured at the substrate of a separate sample; (c) pattern fidelity as a function of FIB dwell time. All data is for the 2.0 μm pattern spacing as measured on the uncapped surface of the six layer sample.

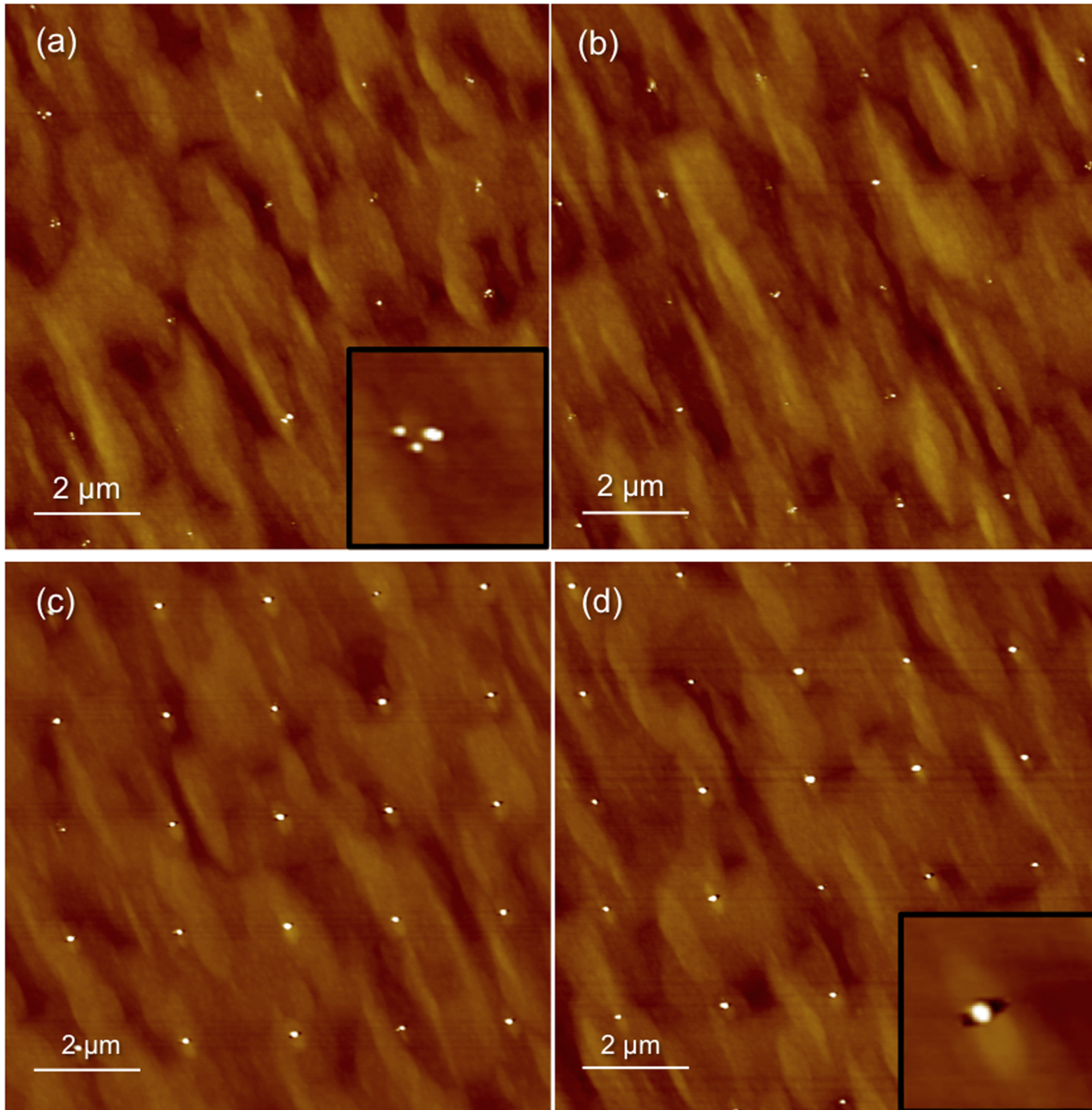

Figure 3.3: AFM images of the uncapped surface of the six layer sample for the 2.0 μm spacing patterns at FIB dwell times of (a) 1.0 ms, (b) 3.0 ms, (c) 6.0 ms, and (d) 9.0 ms. The inset in (a) shows a higher magnification image of the multi-dot nucleation and the inset in (d) shows the concave shape of the FIB pattern, which did not completely planarize upon layering for the 6.0 and 9.0 ms dwell times.

For all FIB dwell times, the original pattern was retained with some level of fidelity despite the relatively thick GaAs spacer layer. This demonstrates that FIB patterning can extend the maximum spacer layer thickness achievable for retaining vertical alignment of QDs, which Xie *et al.* found to be approximately 7 nm for 90-100% strain correlation between layers of unpatterned InAs/GaAs QDs grown with the same InAs deposited thickness we report and at a growth temperature 15 degrees hotter.[21,22] Some researchers have reported vertical QD alignment for spacer layers as thick as 30 nm when the amount of InAs deposited for dot formation was thicker and/or the growth temperature was higher[23,24] than reported here. In this study, the critical thickness for QD nucleation on a planar surface has not been surpassed. Therefore, the vertical QD alignment is not likely to be solely a result of island-induced strain. Instead, it is likely due to the relatively large size of our FIB-induced QDs, which were 5 to 15 nm in height, coupled with any additional strain in the substrate due to FIB patterning. For the longer FIB dwell times, pattern retention may also be due to the concave shape of only partially filled, non-planarized holes, which persisted through to the sixth layer. To further analyze the effects of hole filling on layer-to-layer pattern retention, the fidelity of single and multi-dot formation per patterned site as well as the percentage of empty sites was measured. Figure 3.2 (c) shows the single QD, multi-dot, and empty site fidelities with increasing FIB dwell time for the 2.0 μm pattern spacings. Single QD fidelity increased from only 18% for the 1.0 ms FIB dwell time to nearly 100% for both the 6.0 and 9.0 ms FIB dwell time patterns. The fraction of multi-dot nucleation and empty sites decreased with increasing FIB dwell time, which was likely due to hole filling as previously discussed.

3.3.2 Determination of In Adatom Diffusion Length

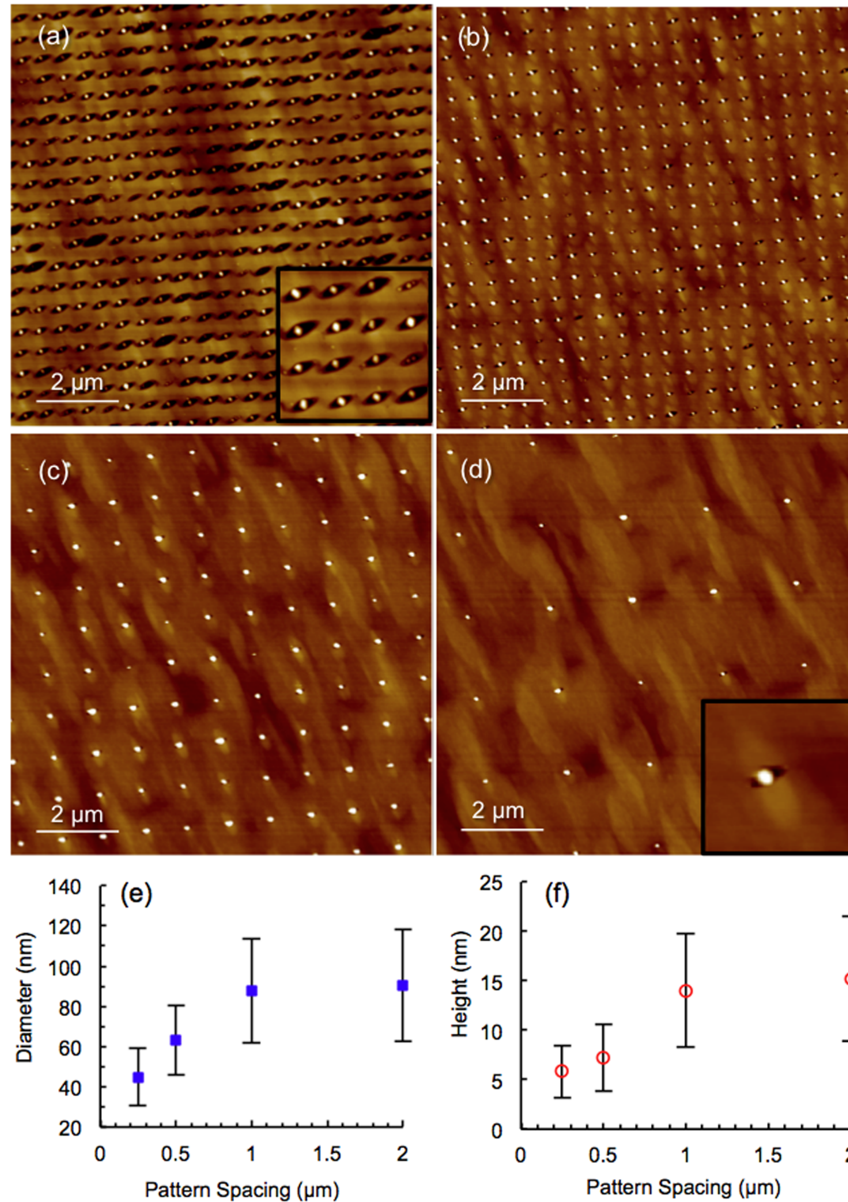

Figure 3.4: AFM images of the uncapped surface of the six layer sample for the 9.0 ms FIB dwell time patterns at pattern spacings of (a) 0.25 µm, (b) 0.5 µm, (c) 1.0 µm, and (d) 2.0 µm. The insert in (a) and (d) show higher magnification images of the QDs. The concave shape of the holes (small, dark area beside the QDs) is shown to persist through to the sixth layer. (e) and (f) Plots of the QD diameter and height as a function of pattern spacing for the 9.0 ms FIB dwell time patterns of the six layer sample.

The pattern spacing was varied from 0.25 to 2.0 μm to analyze its effect on QD size and pattern fidelity. Figure 3.4 (a) – (d) show AFM images of the uncapped sixth layer for the 0.25, 0.5, 1.0, and 2.0 μm pattern spacings at a 9.0 ms FIB dwell time. Varying the pattern spacing did not significantly affect the fidelity of single QDs. However, QD size increased with increasing pattern spacing with the diameter saturating at approximately 90 nm for the 9.0 ms FIB dwell time patterns as shown in the plot in Figure 3.4 (e).

This effect can be explained in terms of the adatom surface diffusion length, which determines the capture zone of the FIB-milled hole.[25,26] For unpatterned surfaces, QD position, size, and areal density are limited in part by the capture zone, which is generally determined by the growth conditions (e.g., temperature and growth rate).[26] However, by creating preferential nucleation sites using the FIB and reducing the thickness of the deposited InAs to below the critical thickness for dot nucleation on a planar surface, QD position and size can instead be controlled by the capture zone of the patterned hole and not the QD. Figure 3.5 (a) and (b) illustrate how the capture zone of the patterned holes changes for large and small pattern spacings. If the pattern spacing is large enough, adatoms moving along the surface can only reach either one or zero FIB-milled holes before coming to rest. Therefore, the adatom diffusion length limits the capture zone of the patterned hole. The volume of InAs available per patterned site, V_{InAs}, for QD nucleation is then determined by the maximum adatom diffusion length, λ, for the given growth conditions and the deposited InAs thickness, t, as

$$V_{InAs} = t\pi\lambda^2 \qquad (1)$$

Therefore, increasing the pattern spacing beyond this distance will not result in a change in QD size without altering the growth conditions (e.g., changing the growth temperature or the deposited InAs thickness). However, as the pattern spacing decreases to less than the maximum

adatom diffusion length, the capture zones of neighboring patterned holes begin to overlap and V_{InAs} is no longer dependent on the maximum diffusion length, but on the pattern spacing, L, as

$$V_{InAs} = tL^2 \qquad (2)$$

The measured QD diameter and height are consistent with this analysis, showing a decrease in size once the pattern spacing decreases below approximately 1.0 μm (figure 4(e)), which is equivalent to a maximum average adatom diffusion length of approximately 500 nm for the given growth conditions.

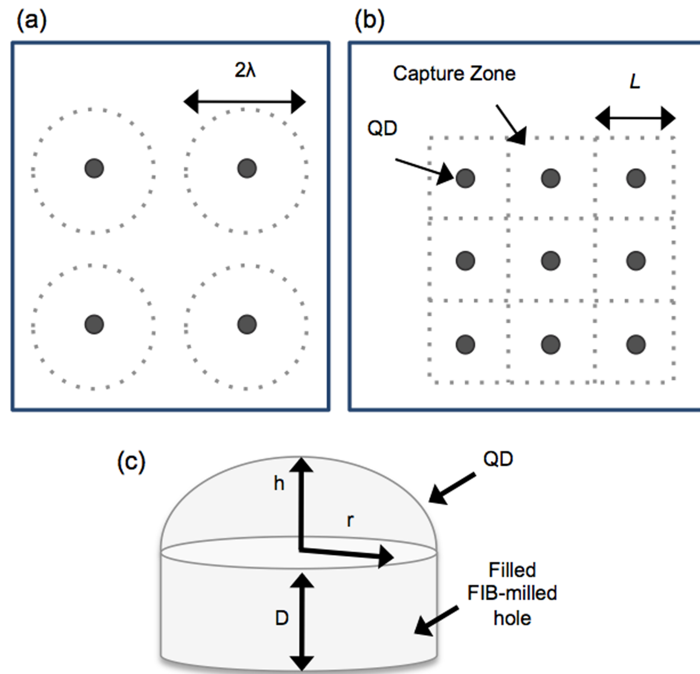

Figure 3.5: Schematics showing the change in the capture zone for (a) close pattern spacings and (b) larger pattern spacings. (c) A schematic of the ellipsoid and cylinder shapes used to approximate the QD volume for the wetting layer thickness estimation.

3.3.3 Variation in Wetting Layer Thickness with Patterning Conditions

The diffusion length at each pattern spacing can be used in conjunction with the measured QD dimensions to estimate the thickness of the WL as a function of pattern spacing.

The minimum thickness of the WL was estimated for the 9.0 ms FIB dwell time patterns at each pattern spacing. The volume of the QD was estimated as half of an ellipsoid (see Figure 3.5 (c)) with an additional volume added to take into account InAs filling of the FIB-milled holes, which were not planarized at the sixth layer for the 9 ms FIB dwell time patterns (see inserts in Figure 3.4). This additional QD volume was estimated as a cylinder (see Figure 3.5 (c)) with height, D, equal to the maximum depth of the FIB-milled holes as measured at the substrate and radius, r, equal to that of the QDs based on observations from the AFM images (see Figure 3.4) such that

$$V_{QD} = \frac{2}{3}\pi r^2 h + \pi r^2 D \tag{3}$$

Although the hole dimensions at the sixth layer may be slightly smaller than at the first layer, using the hole dimensions from the first layer provided an overestimation of the QD volume, ensuring a minimum estimate of the WL thickness. The WL thickness, t_{WL}, is estimated by setting the volume of InAs deposited within the capture zone, V_{InAs}, equal to the sum of the WL and QD (Equation (3)) volumes such that

$$V_{InAs} = (A_{WL} - \pi r^2)t_{WL} + V_{QD} \tag{4}$$

where A_{WL} is the area of the WL and πr^2 is the area of the FIB-patterned hole. For the 1.0 and 2.0 µm pattern spacings, Equation (1) is used for V_{InAs} and A_{WL} is assumed to be a circle (Figure 3.5 (a)) with a radius of 500 nm in accordance with the estimated maximum average adatom diffusion length. For the 0.5 and 0.25 µm pattern spacings, Equation (2) is used for V_{InAs} and A_{WL} is assumed to be a square (Figure 3.5 (b)) with side length equal to the pattern spacing. Solving for t_{WL} gives a WL thickness of approximately 1.4 ML for the 1.0 and 2.0 µm pattern spacings, decreasing to 1.3 and 0.7 ML for the 0.5 and 0.25 µm pattern spacings, respectively. The estimated WL thickness follows the same trend with decreasing pattern spacing as the QD diameter and height (Figure 3.4 (e)), decreasing at a pattern spacing of approximately 1.0 µm.

Some reports have shown changes in QD size and WL thickness upon layering of QDs.[23,27] However, the changes in QD dimensions and WL thickness described in this work are a function of pattern spacing only and are, therefore, independent of layering.

Knowing the maximum average adatom diffusion length is advantageous because it provides an ability to tune the QD and WL dimensions. For example, if the pattern spacing is less than the maximum average diffusion length, QD and WL dimensions can be tailored by altering the pattern spacing. However, if the pattern spacing is greater than the maximum average diffusion length, altering pattern spacing no longer affects QD size so the areal density can be changed without affecting the dimensions of the QDs. This ability to tune QD and WL dimensions by FIB patterning also provides some control over their optical and electronic properties. It is important to note that the adatom diffusion lengths estimated here are for the specific growth and patterning conditions. Therefore, changing these conditions may provide an additional means of adjusting the diffusion length, providing further control over QD properties.

3.3.4 Mound Formation Upon Increased Layering

Increasing the total number of layers of QDs from six to 26 resulted in mound formation above the underlying patterned sites. Figure 3.6 (a) – (d) show AFM images of the uncapped 26th layer for the 0.25, 0.5, 1.0, and 2.0 μm pattern spacings at a 9.0 ms FIB dwell time. At larger pattern spacings, it was evident that mound formation occurred only above the underlying FIB-patterned sites. The mounds were approximately 800-1000 nm in length along $[1\bar{1}0]$, independent of FIB dwell time or pattern spacing. Mounds on the 9.0 ms FIB dwell time patterns had a length/width aspect ratio of approximately three, whereas mounds on the other patterns had a length/width ratio of approximately two. Uncapped surface QDs showed a tendency to form on

the top and sides of the mounds as shown in the insets in Figure 3.6 (c) and (d), which were likely lower energy sites due to an increase in step density. Kiravittaya *et al.* reported mounds aligned along [1$\bar{1}$0] on the uncapped surface of a six layer QD structure patterned by standard optical lithography with a similar spacer thickness (15 nm). They attributed the mounds to the height of the underlying QDs, which was approximately half that of the spacer layer thickness.[18,21] This was likely the case for the 26 layer sample as well, where the average QD height measured after six layers was 15 nm for the largest spacing and 6 nm for the smallest spacing at a 9.0 ms FIB dwell time. These QD heights are a large fraction of the spacer layer thickness, consistent with the hypothesis of Kiravittaya *et al.*

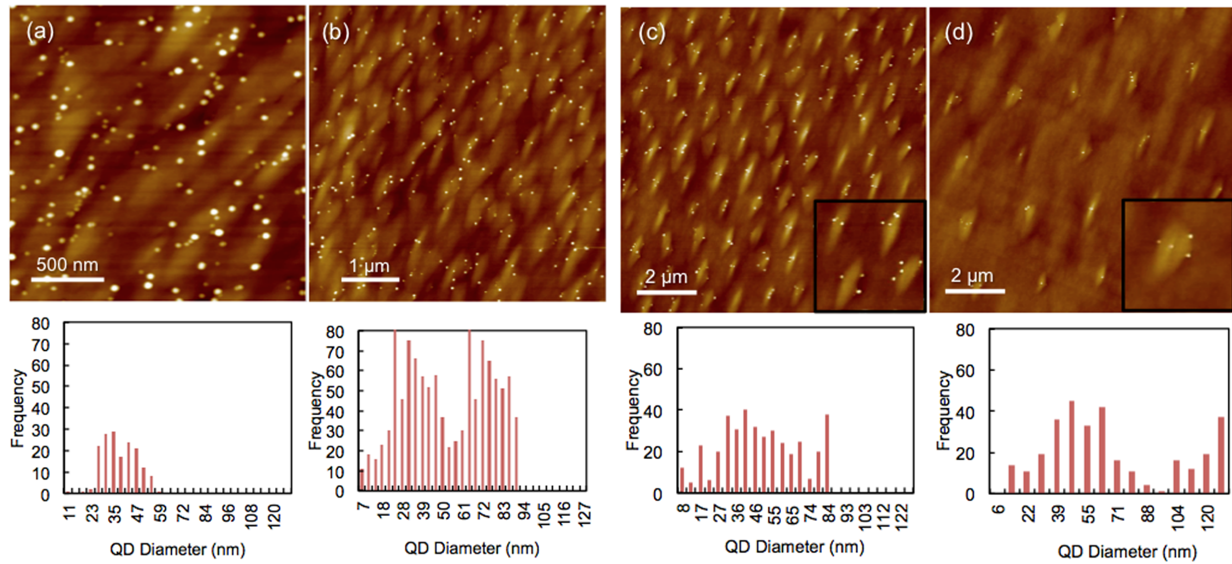

Figure 3.6: AFM images of the uncapped surface of the 26 layer sample for the 9.0 ms FIB dwell time patterns at pattern spacings of (a) 0.25 µm, (b) 0.5 µm, (c) 1.0 µm, and (d) 2.0 µm with a corresponding histogram of QD diameter distribution below each AFM image. The insets in (c) and (d) show higher magnification images of the mounds with QDs on them. The number of bins for each histogram was determined by the square root of the number of data points.

Although QDs formed on the mounds and retained the general periodicity of the original patterns for the 1.0 and 2.0 μm pattern spacings, the mounds are undesirable for several reasons. For closer pattern spacings, mound proximity destroyed fidelity as seen in Figure 3.6 (a) and (b). Because the maximum lateral dimension of the mounds is ~1 μm, the closest pattern spacing achievable without disrupting the pattern is ~0.7 μm when the pattern is oriented 45° off [1$\bar{1}$0]. Spacings as small as 0.3 μm can be achieved if the mounds are aligned along [1$\bar{1}$0] and allowed to overlap along that direction.[18,21] However, control over QD position would suffer along the ridge forming from the overlapping mounds. In either case, mounds limit the highest achievable QD density and control over QD position. Interestingly, QD density vs. pattern spacing still followed the theoretical trend for QD density vs. pattern spacing despite the loss of pattern fidelity. Figure 3.7 shows the QD density measured on the 26th layer as a function of pattern spacing and dwell time and dashed, dotted, and solid lines for theoretical densities assuming two, four, and 12 QDs per patterned site, respectively. As the FIB dwell time increased, the fidelity of mound formation above the underlying holes also increased. Because QDs tended to form only on the mounds and multiple dots formed per mound, the theoretical number of QDs per patterned site increased with increasing FIB dwell time. However, the 9.0 ms FIB dwell time corresponded to a theoretical density of two QDs/site instead of following the increasing trend. This is due to the smaller length/width aspect ratio of mounds on the 9.0 ms FIB dwell time, resulting in a lower step edge area per mound and a lower QD areal density for the 9.0 ms FIB dwell time pattern. Additionally, mound formation created multiple preferred nucleation sites per each FIB-patterned site, hindering control over QD density and position. Finally, a bimodal QD size distribution of the uncapped surface dots was measured via AFM. Histograms of the QD diameter distributions are shown in Figure 3.6 for the 9.0 ms FIB dwell time patterns at each

pattern spacing. The number of bins for each histogram was determined by the square root of the number of data points for the given pattern.

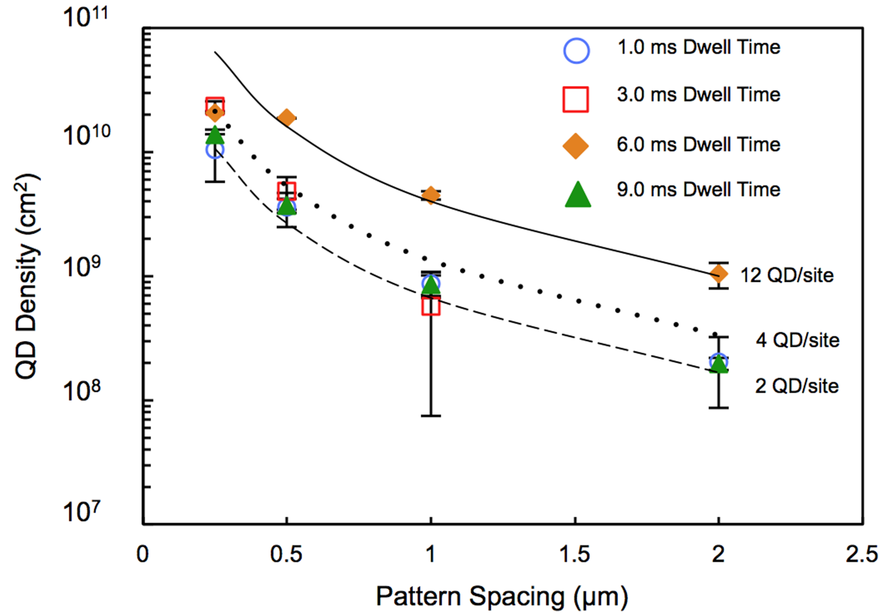

Figure 3.7: Plot of the QD areal density as a function of pattern spacing as measured on the uncapped surface of the 26 layer sample for the 9.0 ms FIB dwell time. Error bars are not visible for all data points due to a small standard deviation for some of the measurements. The dashed and solid lines are explained in the text.

The bimodal size distribution was also evidenced by a split QD peak in the photoluminescence (PL) data. Figure 3.8 shows the PL spectra for the 9.0 ms FIB dwell time patterns at each pattern spacing. The sample was mounted in a helium flow cryostat at 15 K and pumped using a 633 nm helium-neon laser with 282.5 μW incident power focused through a 0.7 NA infinity corrected objective. The PL spectra were collected using a 0.75 m spectrometer with a 150 G/mm reflection grating and a single channel InGaAs detector. The GaAs substrate peak is at 1.49 eV, and the WL peak is at 1.43 eV. The QD peak, which splits for spacings larger than 0.25 μm, is between 1.27 and 1.35 eV. The separation between the QD PL peaks increased with

increasing pattern spacing, which corresponded to the increased separation of the average QD size as measured by AFM. Additionally, as the pattern spacing increased, the intensity of the QD peaks decreased while the WL peak intensity increased relative to the GaAs peak due to the lower QD density and larger WL area at larger pattern spacings.[19]

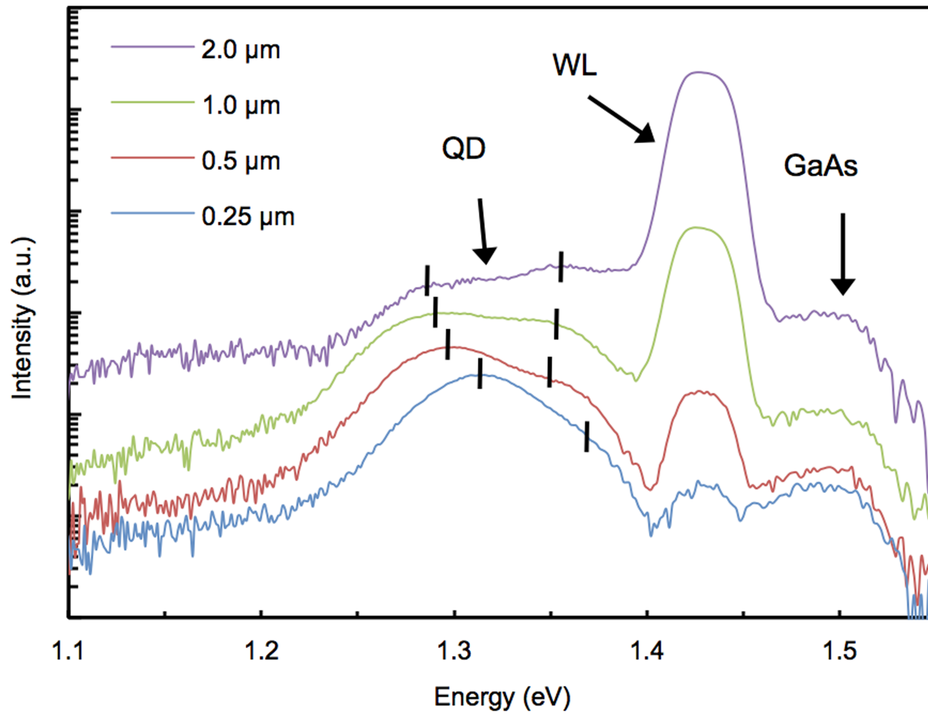

Figure 3.8: Photoluminescence spectrum from the 26 layer sample for the 9.0 ms FIB dwell time patterns showing the GaAs substrate peak at 1.49 eV, the wetting layer peak at 1.43 eV, and the QD peak between 1.27 and 1.35 eV. The split QD peak is a result of the bimodal QD distribution. The peak positions for the split QD peak are indicated by the tick marks. Measurements were taken at 15 K. Data collected by Timothy W. Saucer and Garrett V. Rodriguez, Prof. Vanessa Sih group, Physics Department, University of Michigan.

3.4 Conclusions

In conclusion, this study demonstrates the ability to control QD position and size via *in vacuo* FIB patterning while varying pattern spacing and hole size with up to 100% single QD per